

Revisiting the formaldehyde masers II: effects of an H II region and beaming

D.J. van der Walt [★]

Centre for Space Research, North-West University, Hoffman Street, 2520, Potchefstroom, South Africa

Accepted 2024 September 16. Received 2024 September 13; in original form 2024 June 19

ABSTRACT

We present new results of a numerical study of the pumping of 4.8 GHz and 14.5 GHz maser of o-H₂CO in the presence of a free-free radiation field. It is shown that in the presence of a free-free radiation field inversion of not only the $1_{10} - 1_{11}$, but also the $2_{11} - 2_{12}$ and other doublet state transitions occur. Further results are presented to illustrate how, as a consequence of the pumping scheme, the inversion of the $1_{10} - 1_{11}$ and $2_{11} - 2_{12}$ transitions respond to the free-free radiation fields associated with H II regions with different emission measures and levels of geometric dilution with respect to the masing region. We also discuss the criticism raised in the past by various authors against the pumping of the 4.8 GHz H₂CO masers by a free-free radiation field. It is argued that the rarity of the H₂CO masers is not to be ascribed to the pumping scheme but to other factors such as, e.g., the evolution of the associated H II region or the chemical evolution of the star forming region which determines the H₂CO abundance or a combination of both.

Key words: masers – stars:formation – ISM:molecules – radio lines:ISM – H II regions

1 INTRODUCTION

Following the discovery of the first 4.8 GHz o-H₂CO (henceforth H₂CO) maser in NGC 7538 by [Downes & Wilson \(1974\)](#), [Boland & de Jong \(1981\)](#) presented the first model to explain such maser emission. [Boland & de Jong \(1981\)](#) showed that the $1_{10} - 1_{11}$ transition can be inverted by the free-free radiation field of a compact H II region. Since the model by [Boland & de Jong \(1981\)](#) was the only one for many years, various authors tested the model against their observations. Authors such as, for example, [Gardner et al. \(1986\)](#), [Mehring et al. \(1994\)](#), [Martín-Pintado et al. \(1999\)](#), [Hoffman et al. \(2003\)](#) and [Araya et al. \(2007\)](#) concluded that the H₂CO masers known at the time these papers were published, did not meet the conditions required by the model of [Boland & de Jong \(1981\)](#) and, therefore, that the pumping of the 4.8 GHz H₂CO masers by a free-free radiation field is not a viable mechanism to explain the masers. Some of the reasons for dismissing the model of [Boland & de Jong \(1981\)](#) are, that the emission measures (EM) of the H II regions with which some of the 4.8 GHz H₂CO masers are associated, are smaller than the lower limit of 10^8 pc cm^{-6} for which [Boland & de Jong \(1981\)](#) found an inversion, and that some of the masers are, according to the results of [Boland & de Jong \(1981\)](#), offset too far from the H II regions to explain the inversion by a free-free radiation field. The apparent failure of the [Boland & de Jong \(1981\)](#) model to explain the H₂CO masers prompted [Hoffman et al. \(2007\)](#) to postulate that some rare collisional process may be responsible for the pumping of the masers. Based on their observations of G339.88-1.26, [Chen et al. \(2017b\)](#) argued in favour of the collisional excitation in a jet/outflow driven shock of the $1_{10} - 1_{11}$ H₂CO masers. Still more recently, [McCarthy et al. \(2022\)](#) also express the opinion that the pumping

mechanism for the population inversion of the $1_{10} - 1_{11}$ transition of H₂CO is poorly understood.

Another outstanding question to be addressed is the apparent absence of the 14.5 GHz ($2_{11} - 2_{12}$) H₂CO maser which, according to the model of [Boland & de Jong \(1981\)](#), should be associated with the 4.8 GHz maser if the pumping is through a free-free radiation field. [Hoffman et al. \(2003\)](#) concluded that the non-detection or absence of the 14.5 GHz maser possibly indicates particular physical conditions for the excitation of the 4.8 GHz masers. Recently, [Chen et al. \(2017a\)](#) reported the detection of 14.5 GHz emission from three high mass star forming regions which have associated 4.8 GHz H₂CO masers. These authors consider the 14.5 GHz emission associated with NGC 7538 to be maser emission, although [Shuvo et al. \(2021\)](#) argues that it might be thermal rather than maser emission. Independent of whether the 14.5 GHz emission in NGC7538 is maser or thermal emission, it is clear that, apart from understanding the inversion of the $1_{10} - 1_{11}$ transition, it is also necessary to understand the behaviour of the $2_{11} - 2_{12}$ transition.

A further question related to the H₂CO $1_{10} - 1_{11}$ masers is the rarity of these masers. Counting individual masers, e.g. two components associated with NGC 7538, two with G29.96-0.02, nine with Sgr B2, to date only 21 such masers have been detected in the Galaxy ([Downes & Wilson 1974](#); [Whiteoak & Gardner 1983](#); [Mehring et al. 1994](#); [Pratap et al. 1994](#); [Araya et al. 2005, 2006, 2008, 2015](#); [Ginsburg et al. 2015](#); [Chen et al. 2017b](#); [McCarthy et al. 2022](#)). While the rarity of the masers may be related to the pumping mechanism, as proposed by [Hoffman et al. \(2007\)](#), there are also other possibilities which can explain the rarity of the masers. As one of a number of possibilities, [Ginsburg et al. \(2015\)](#) also consider a short life-time of the masers as a possible explanation of the rarity of the $1_{10} - 1_{11}$ masers. Factors that might determine the life-time of the masers are, for example, the chemical, dynamical and radiative (dust

[★] E-mail: johan.vanderwalt@nwu.ac.za

and free-free) evolution of the star forming environment. The pumping scheme, however, is determined exclusively by the molecular structure and not any external macroscopic factors. Whether or not a certain transition is inverted depends on its interaction (collisional and radiative) with its environment.

In a recent paper, *van der Walt & Mfulwane (2022)* presented the results of a non-LTE study on the inversion of the $1_{10} - 1_{11}$ transition of H_2CO . The focus of these authors was primarily on understanding the claim by *Baan et al. (2017)* that the extragalactic megamasers associated with three ultraluminous infrared (starburst) galaxies are radiatively pumped by dust emission, as well as expanding on the results of *van der Walt (2014)* by increasing the parameter space in kinetic temperature and H_2 density. These authors showed that inversion of the $1_{10} - 1_{11}$ transition can be achieved from collisions alone, and that, in the presence of a far-infrared dust radiation field, inversion does not take place when collisions are excluded. *van der Walt & Mfulwane (2022)* also proposed a pumping scheme which can explain why, in the case where the external radiation field is only that of dust, collisions are required for the inversion of the $1_{10} - 1_{11}$ transition.

The context of the present calculations is a pumping calculation with the aim to, first, establish whether the pumping scheme proposed by *van der Walt & Mfulwane (2022)* applies to the case of excitation by a free-free radiation field. It is further investigated to what extent the $1_{10} - 1_{11}$ and $2_{11} - 2_{12}$ transitions are inverted by different free-free radiation fields and what the effect of beaming is. We also comment on past critique against the viability of the pumping of the masers by a free-free radiation field. Although it is necessary to try to reproduce the optical depths of the $1_{10} - 1_{11}$ transition as derived from observations (for example in *Hoffman et al. 2003*), the aim of the present calculations is not to explain individual sources.

2 NUMERICAL METHOD

The numerical method used for the present calculations is the same as that described in detail by *van der Walt et al. (2021)* and *van der Walt & Mfulwane (2022)* and will therefore not be repeated here. The molecular data used is also the same as that described in *van der Walt & Mfulwane (2022)*. We assumed a constant density and temperature H II region to calculate the free-free continuum radiation field given by

$$F_\nu(T_e) = B_\nu(T_e)(1 - e^{-\tau_\nu}). \quad (1)$$

$B_\nu(T_e)$ is the Planck function, T_e the electron temperature, and τ_ν the frequency dependent optical depth given by

$$\tau_\nu = 8.235 \times 10^{-2} \left(\frac{T_e}{\text{K}}\right)^{-1.35} \left(\frac{\nu}{\text{GHz}}\right)^{-2.1} \left(\frac{\text{EM}}{\text{pc cm}^{-6}}\right) \quad (2)$$

(*Wilson et al. 2009*). EM is the emission measure and is given by

$$\text{EM} = \int_{r_{\text{inner}}}^{r_{\text{outer}}} \left(\frac{n_e(r)}{\text{cm}^{-3}}\right)^2 d\left(\frac{r}{\text{pc}}\right). \quad (3)$$

with n_e the electron density.

An important factor in the present calculations is the geometric dilution of the free-free radiation field. The geometric dilution factor, $W_{\text{H II}}$ is defined as the ratio of the solid angle, ω , subtended by the H II region at the location of the masing gas, relative to the total solid angle 4π . Assuming a spherical H II region and expressing ω in terms of the radius, $R_{\text{H II}}$, of the H II region and the distance, r , from

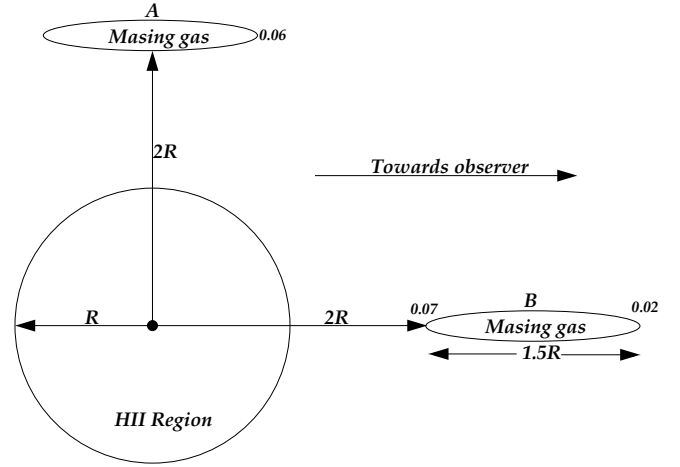


Figure 1. Schematic illustration of two possible positions of the masing gas relative to the H II region with radius R . For case A the centre of the masing region, with linear dimension of $1.5R$, is at a distance $2R$ from the centre of the H II region which corresponds to $W_{\text{H II}} = 0.07$. At the right hand end of the masing volume $W_{\text{H II}} = 0.06$. In case B the masing region is projected against the H II region such that the left hand end is at distance $2R$ from the centre of the H II region. The right hand end is at $3.5R$ from the centre of the H II region where $W_{\text{H II}} = 0.02$.

the centre of the H II region, the distance dependent dilution factor is given by

$$W_{\text{H II}}(r) = \frac{1}{2} \left\{ 1 - \sqrt{1 - \left(\frac{R_{\text{H II}}}{r}\right)^2} \right\}. \quad (4)$$

For the case when $r \gg R_{\text{H II}}$ it follows that

$$W_{\text{H II}}(r) \sim \frac{1}{4} \left(\frac{R_{\text{H II}}}{r}\right)^2. \quad (5)$$

From Eq. 4 it follows that $W_{\text{H II}} = 0.5$ when $r = R_{\text{H II}}$, and that $W_{\text{H II}}$ is therefore restricted to values ≤ 0.5 . For all practical purposes one can say that Eq. 5 applies for $r > 5R_{\text{H II}}$ in which case $W_{\text{H II}} < 0.01$.

Within the framework of the escape probability method, and for an inverted transition, beaming is taken into account by modifying the escape probability

$$\beta_\nu = \frac{e^{\tau_\nu} - 1}{\tau_\nu} \quad (6)$$

to become

$$\beta_\nu(\tau) = \frac{\Omega_\nu(\tau)}{4\pi} \frac{e^{\tau_\nu} - 1}{\tau_\nu} \quad (7)$$

where Ω_ν is the frequency dependent beaming angle (see Section 5.3 of *Elitzur 1992*). According to *Elitzur (1992, Section 5.1.3)*, the beaming solid angle varies as ℓ^{-1} for unsaturated masers and as ℓ^{-2} for saturated masers, where ℓ is the length along the ray path. Since $\tau \propto \ell$, it was assumed that

$$\frac{\Omega_\nu(\tau_\nu)}{4\pi} = \frac{1}{(\alpha_\nu \tau_\nu + 1)^2} \quad (8)$$

as an approximation of such behaviour. Thus,

$$\beta_\nu(\tau) = \frac{1}{(\alpha_\nu \tau_\nu + 1)^2} \frac{e^{\tau_\nu} - 1}{\tau_\nu}. \quad (9)$$

It should be noted, however, that e^τ increases faster than what τ^{-2} decreases for $\tau \gtrsim 1$ and, therefore, that $\beta_\nu(\tau)$ increases toward larger values of τ rather than to decrease. Inspection of the behaviour of $\beta_\nu(\tau)$ (as in Eq. 9) has further shown that $\beta_\nu(\tau)$ has a power law behaviour of the form $\alpha\tau^{-\gamma}$ for $0.4 < \tau \leq 1$ for $\alpha \geq 1$. To avoid the escape probability to increase for $\tau > 1$, it was assumed that the power law behaviour continues for $\tau > 1$. The power law index, γ , depends on α_ν ; for example, $\gamma = -0.41, -1.15$, and -1.36 respectively for $\alpha = 1, 5$ and 10 .

Although it is not the explicit intention of the calculations to model specific maser sources, it is necessary to use beaming angles that correspond to observed 4.8 GHz maser spot sizes. Consider therefore a maser spot at a distance d from the observer and which has an angular size of θ radians. The surface area of the spot is then $A = \pi d^2 \theta^2 / 4$. On the other hand, for a maser path length ℓ_m and a beaming angle Ω given by Eq. 8, the cross sectional area of the cone is $A = 4\pi \ell_m^2 / (\alpha\tau + 1)^2$. Equating the two areas, it follows that

$$\alpha\tau = \frac{4\ell_m}{\theta d} - 1 \quad (10)$$

To illustrate the application of Eq. 10 consider, for example, the case of G29.96-0.02. Hoffman et al. (2003) measured the angular size of the two maser components to be ~ 19 milli-arcseconds at a distance of 6.5 kpc. For a maser path length of 7×10^{16} cm (to be discussed later) we have $\alpha\tau = 150$. Choosing, for example, $\alpha = 15$ implies that for $\tau = 10$ the angular diameter of the spot will agree with the observed angular diameter.

The present calculations are done within the framework of the escape probability method which requires that the physical conditions, e.g. density, temperature and the free-free radiation field, be uniform over the length of the masing column. To meet this requirement all parts of the masing volume of gas should be almost equidistant from the H II region. The implied geometry is therefore a volume of gas with length ℓ_m illuminated from the side with the free-free emission from a hyper- or ultra-compact H II region, schematically illustrated as case A in Fig. 1. The masing region can also be located as in case B. In this scenario there is a gradient in the geometric dilution of the free-free radiation field across the length of the masing region which means non-uniform pumping rates between the two end points of the masing region. Case B is certainly the more realistic scenario but cannot be dealt with using the escape probability method. Case A is, however, sufficient to investigate to what extent the free-free radiation field can lead to the inversion of the $1_{10} - 1_{11}$ and $2_{11} - 2_{12}$ transitions. Case A is qualitatively similar to the LVG method for a uniform source as was used by Cragg et al. (2002) to study the pumping of CH₃OH masers.

3 PUMPING SCHEME

In brief, the pumping scheme proposed by van der Walt & Mfulwane (2022) is as follows: In the presence of a far-infrared radiation field radiative excitation out of 1_{11} into the ladders of lower and upper doublet states is asymmetric. This follows from the fact that although the Einstein B-coefficients for the transitions $1_{11} \rightarrow 1_{10}$ (4.8 GHz) and $1_{11} \rightarrow 2_{12}$ (140.8 GHz) are almost equal, the spectral energy density at 140.8 GHz is significantly larger than at 4.8 GHz for a typical far-infrared radiation field of the form $F_\nu(T_d) = (1 - \exp(-\nu/\nu_0)^p) B_\nu(T_d)$ with e.g. $T_d \sim 50$ to 100 K, $p = 1.8$, and $\nu_0 \sim 10^{12}$ Hz. Thus, radiative excitation out of 1_{11} will therefore populate the ladder of lower double states faster than the ladder of upper doublet states. Using the collision coefficients

of the Leiden Atomic and Molecular Database (Schöier et al. 2005) it is rather straight forward to show, for collisions with both o - H₂ and p - H₂, that there is a slight asymmetry which favours collisional excitation from 1_{11} into the ladder of lower doublet states and that the asymmetry increases with increasing kinetic temperature. To create an inversion of the $1_{10} - 1_{11}$ transition, it is necessary to transfer molecules from the ladder of lower doublet states to the ladder of upper doublet states. For the case where excitation is through a far-infrared radiation field and collisions, the transfer of molecules from the ladder of lower doublet states to the ladder of upper doublet states is collisional as was shown by van der Walt & Mfulwane (2022).

To illustrate the pumping scheme in the presence of a free-free radiation field (but also for later examples) four emission measures were chosen such that the turnover frequencies of the free-free radiation fields correspond to the frequencies for the $3_{12} - 3_{13}$ (28.9 GHz), $4_{13} - 4_{14}$ (48.3 GHz), $5_{14} - 5_{15}$ (72.4 GHz) and, $6_{15} - 6_{16}$ (101.3 GHz) doublet transitions. The turnover frequencies therefore correspond to transitions where molecules can be transferred from the ladder of lower doublet states to the ladder of upper doublet states. The associated emission measures (with units of pc cm⁻⁶) are respectively 2.46×10^9 , 7.19×10^9 , 1.69×10^{10} and 3.41×10^{10} . The respective spectral energy density distributions are shown in Fig. 2 where, in the upper panel $W_{\text{H II}} = 0.5$ for all four emission measures and in the lower panel for different dilution factors such that the spectral energy densities at 1000 GHz are the same as for EM = 2.46×10^9 pc cm⁻⁶ with $W_{\text{H II}} = 0.5$. This means that $W_{\text{H II}} = 0.171$ for EM = 7.19×10^9 pc cm⁻⁶, $W_{\text{H II}} = 0.073$ for EM = 1.69×10^{10} pc cm⁻⁶ and, $W_{\text{H II}} = 0.036$ for EM = 3.41×10^{10} pc cm⁻⁶. The upper and lower panels of Fig. 2 therefore represent two special cases where, for the upper panel, the excitation rates (which are directly proportional to the spectral energy density, Eq. 11) for $\Delta J = 1, \Delta K_C = 1$ transitions within the ladder of lower doublet states (lines 1 to 5) range approximately over an order of magnitude from EM = 2.46×10^9 pc cm⁻⁶ to EM = 3.41×10^{10} pc cm⁻⁶. On the other hand, the $\Delta J = 0, \Delta K_C = -1$ transition rates for the three lowest doublet states (lines 6, 7, 8) are approximately the same for the four emission measures. In the lower panel the situation is reversed, that is, the excitation rates within the ladder of lower doublet states (lines 1 to 5) are practically the same for the four emission measures while there are marked differences for the $\Delta J = 0, \Delta K_C = -1$ transitions for the transfer of molecules from the ladder of lower doublet states to the ladder of upper doublet states. Also shown in both panels is the spectral energy density distribution for a far-infrared radiation field for $T_d = 100$ K and a dilution factor of 0.5.

For radiative excitation out of 1_{11} there are, as mentioned above, two possibilities, viz. $1_{11} \rightarrow 1_{10}$ (4.8 GHz - dashed blue vertical line 6) and $1_{11} \rightarrow 2_{12}$ (140.8 GHz - dashed red vertical line 1). Due to the significant difference in the spectral energy densities at these two frequencies, radiative excitation rate from $1_{11} \rightarrow 2_{12}$ is higher than from $1_{11} \rightarrow 1_{10}$, resulting in a faster population of the ladder of lower doublet states compared to the ladder of upper doublet states. Further excitation within the ladder of lower doublet states, for example, $2_{12} \rightarrow 3_{13} \rightarrow 4_{14} \rightarrow 5_{15} \rightarrow 6_{16}$ are facilitated through absorption of photons respectively at frequencies indicated by the vertical dashed red lines 2, 3, 4, 5. The transfer of molecules from the ladder of lower doublet states to the ladder of upper doublet states, for example $2_{12} \rightarrow 2_{11}, 3_{13} \rightarrow 3_{12}$ etc, is through the absorption of photons at frequencies indicated by the vertical dashed blue lines 7 to 11.

The important point to be established is whether the transfer of molecules from the ladder of lower doublet states to the ladder of upper doublet states is essential for an inversion of the $1_{10} - 1_{11}$

transition. The radiative transition rate between a lower and an upper state is given by

$$\Gamma_{lu} = B_{lu}U_{ul} = \frac{g_u}{g_l} \frac{c^3}{8\pi h\nu_{ul}^3} A_{ul}U_{ul}. \quad (11)$$

where U_{ul} is the spectral energy density of the free-free radiation field at the frequency ν_{ul} . Γ_{lu} can be changed by changing either A_{ul} or U_{ul} . To test whether the inversion of the $1_{10} - 1_{11}$ transition depends on the rate at which molecules are transferred from the ladder of lower doublet states to the ladder of upper doublet states ($\Delta J = 0, \Delta K_c = -1$), it is necessary to only change the rates of these transitions while keeping the rates for all other transitions the same. The simplest way to do this is by adjusting, with the exception of the $1_{11} \rightarrow 1_{10}$ transition (through which molecules are radiatively excited into the ladder of upper doublet states), the Einstein A-coefficients for the $\Delta J = 0, \Delta K_c = \pm 1$ transitions rather than modifying the radiation field.

Figure 3 shows an example of the variation of $\tau_{4,8}$ with specific column density when (a) the “standard” A-coefficients for the $\Delta J = 0, \Delta K_c = \pm 1$ transitions are used (black line), (b) when all the coefficients are set to be of the order of 10^{-15} s^{-1} (dashed blue line) (c) when the standard coefficients are reduced by a factor of 100 (solid blue line), (d) when the standard coefficients are reduced by a factor of 50 (dashed black line), (e) when standard coefficients are increased by one and two orders of magnitude above their standard values (red and green lines respectively). The A-coefficients for all the other allowed transitions were kept at their “standard” values. Reducing the A-coefficients for the $\Delta J = 0, \Delta K_c = \pm 1$ transitions to be of the order of 10^{-15} s^{-1} , implying that there is virtually no exchange of molecules between the ladder of lower doublet states and the ladder of upper doublet states, has as consequence that there is no inversion of the $1_{10} - 1_{11}$ transition for specific column densities less than $\sim 8 \times 10^{11} \text{ cm}^{-3} \text{ s}$. The small inversion that follows can be shown to be due to collisional transfer of molecules between the ladders of lower and upper doublet states. The trends in the behaviour of $\tau_{4,8}$ for the different cases shown in Fig. 3 clearly show that the inversion of the $1_{10} - 1_{11}$ transition depends on the transfer of molecules from the ladder of lower doublet states to the ladder of upper doublet states. The pumping scheme proposed by [van der Walt & Mfulwane \(2022\)](#), as explained above, therefore also applies when excitation is due to a free-free radiation field, the difference being that in the presence of a free-free radiation field the pumping is dominantly radiative.

Comparing the spectral energy density distributions in both panels of Fig. 2 clearly shows that for the far-infrared radiation field the spectral energy densities responsible for the excitation from 1_{11} into the ladder of lower doublet states (dashed vertical red lines 1 to 5) are significantly smaller (in some cases more than an order of magnitude) than for the free-free radiation fields. It is also seen for the far-infrared radiation field, that the spectral energy densities at the frequencies responsible for the transfer of molecules from the ladder of lower doublet states to the ladder of upper doublet states (dashed vertical blue lines 6 to 11) are many orders of magnitude smaller than for the free-free radiation fields. The dust radiation field therefore plays a completely insignificant role in the pumping of the masers in regions where the free-free radiation field dominates.

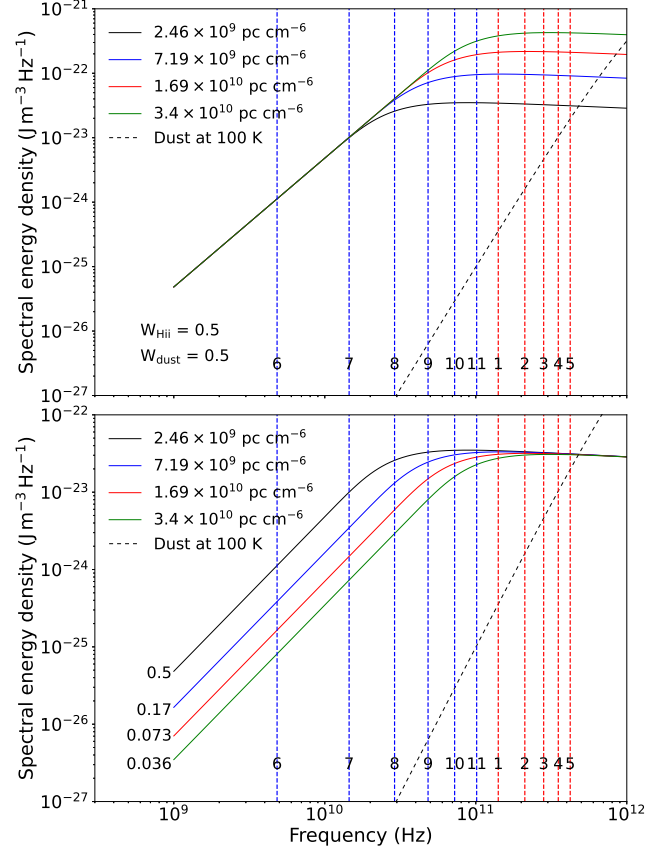


Figure 2. *Upper panel:* Theoretical spectral energy density distributions for four HII regions with emission measures and dilution factor as shown. The vertical dashed red lines numbered 1 to 5 correspond respectively to the first five $\Delta J = 1, K_a = 1, \Delta K_c = 1$ transitions in the ladder of lower doublet states with frequencies 140.84, 211.21, 281.53, 351.77 and, 421.92 GHz. The vertical dashed blue lines numbered 6 to 11 correspond respectively to the first five $\Delta J = 0, K_a = 1, \Delta K_c = -1$ transitions from the ladder of lower doublet states to the ladder of upper doublet states with frequencies 4.83, 14.49, 28.97, 48.28 and, 72.41 GHz. *Bottom panel:* Same as for the upper panel but with the spectral energy densities normalized at 10^3 GHz to that for $EM = 2.46 \times 10^9 \text{ pc cm}^{-6}$ with $W_{\text{HII}} = 0.5$. The resulting dilution factors associated with each emission measure are shown on the graph.

4 ILLUSTRATIVE EXAMPLES

4.1 Basic results without beaming

The basic result of the calculational procedure to solve for the level populations is the variation of the level populations, and therefore also quantities such as the optical depth and the excitation temperature, as a function of the H_2CO specific column density as described in [van der Walt et al. \(2021\)](#). As a first illustrative result, the variation of the optical depth for the $1_{10} - 1_{11}$ ($\tau_{4,8}$) and $2_{11} - 2_{12}$ ($\tau_{14,5}$) transitions in the presence and absence of a free-free radiation field are compared in the upper panel of Fig. 4. The results were obtained for $n_{\text{H}_2} = 10^5 \text{ cm}^{-3}$, $T_k = 180 \text{ K}$, an H_2CO abundance ($X_{\text{H}_2\text{CO}}$) of 5.0×10^{-6} , a maser linewidth of 0.3 km s^{-1} , $EM = 3 \times 10^{10} \text{ pc cm}^{-6}$ and $W_{\text{HII}} = 0.5$. The lower panel shows the corresponding variation of the excitation temperatures for the two transitions where negative excitation temperatures indicate a population inversion. It is seen that in the absence of a free-free radiation field, the $1_{10} - 1_{11}$ transition is not inverted up to a specific column density of $\sim 4 \times 10^{11} \text{ cm}^{-3} \text{ s}$.

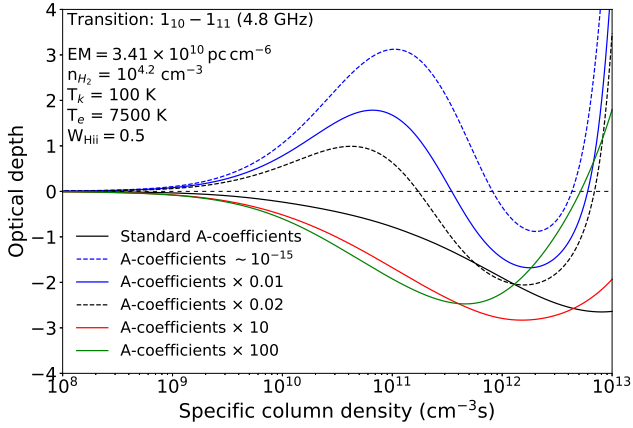


Figure 3. Comparison of the variation of the optical depth of the $1_{10} - 1_{11}$ transition as function of specific column density where the Einstein A-coefficients for the doublet state transitions ($\Delta J = 1, \Delta K_c = \pm 1$) have been adjusted to illustrate the effect of changing the rate of transfer of molecules from the ladder of lower doublet to the ladder of upper doublet states.

The $2_{11} - 2_{12}$ transition is not inverted, which was more generally found to hold for all combinations of n_{H_2} and T_k where the $1_{10} - 1_{11}$ transition is inverted in the absence of a free-free radiation field. In the presence of a strong free-free radiation field (minimum geometric dilution) both transitions are seen to be inverted, even at those specific column densities where the $1_{10} - 1_{11}$ transition is not inverted in the absence of a free-free radiation field.

Since, as was shown in Section 3, the inversion of the $1_{10} - 1_{11}$ transition can be achieved through the pumping by a free-free radiation field, it can be expected that $\tau_{4,8}$ and $\tau_{14,5}$ depend on the emission measure and the dilution factor, W_{HII} . The variation of $\tau_{4,8}$ and $\tau_{14,5}$ as a function of the specific column density for the two scenarios shown in the upper and lower panels of Fig. 2 is shown respectively in Figs. 5 and 6 with $n_{\text{H}_2} = 10^{4.2} \text{ cm}^{-3}$, $T_k = 100 \text{ K}$ and, $T_e = 7500 \text{ K}$. It is worth keeping in mind that, from Eq. 4, the dilution factors of 0.5, 0.171, 0.073 and 0.036 correspond respectively to distances of $1.0R_{\text{HII}}$, $1.3R_{\text{HII}}$, $1.9R_{\text{HII}}$ and, $2.7R_{\text{HII}}$ from the centre of the H II region.

Comparison of Figs. 5 and 6 shows some obvious differences. For example, in Fig. 5 it is seen that there is very little difference in $\tau_{4,8}$ for the different emission measures for specific column densities up to $\sim 3 \times 10^{11} \text{ cm}^{-3} \text{ s}$. This can partly be ascribed to the transition rates being equal (or approximately equal) for the first three $\Delta J = 0, \Delta K_c = -1$ transitions (lines 6, 7 and 8 in the upper panel of Fig. 2) although the excitation rates into and within the ladder of lower doublet states (lines 1 to 5 in the upper panel of Fig. 2) differ significantly. On the other hand, when the dilution factors for the four emission measures are different, as in the lower panel of Fig. 2, the variation of $\tau_{4,8}$ with specific column density as shown in Fig. 6 is quite different from that in Fig. 5. In fact, it is seen in Fig. 6 that the maximum of $\tau_{4,8}$ for $\text{EM} = 3.41 \times 10^{10} \text{ pc cm}^{-6}$ at a distance of $2.7R_{\text{HII}}$ is greater than for $\text{EM} = 2.46 \times 10^9 \text{ pc cm}^{-6}$ with the masing region located at the edge of the H II region. Also, closer inspection of the upper panel of Figs. 5 shows that $\tau_{4,8}$ is greater for $\text{EM} = 2.46 \times 10^9 \text{ pc cm}^{-6}$ than for $\text{EM} = 3.41 \times 10^{10} \text{ pc cm}^{-6}$ for specific column densities less than $\sim 3 \times 10^{11} \text{ cm}^{-3} \text{ s}$. At first sight, this behaviour appears to be counter intuitive since, if the masing region is closer to the H II region, pumping might be expected to be more effective to establish a larger inversion of the $1_{10} - 1_{11}$ transition.

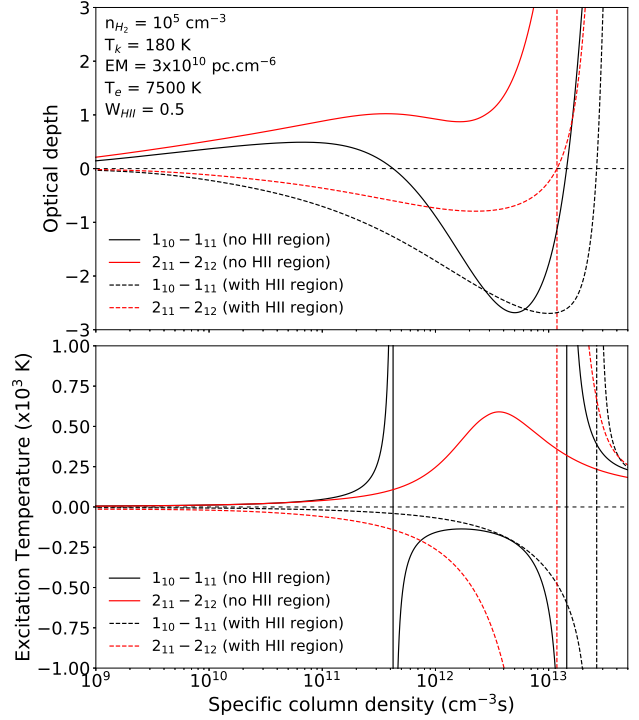


Figure 4. *Upper panel:* Comparison of the variation of the optical depth as function of specific column density for the $1_{10} - 1_{11}$ and $2_{11} - 2_{12}$ transitions in the absence of a free-free radiation field with the case when a free-free radiation field is present. *Bottom panel:* Comparison of the variation of the excitation temperature for the $1_{10} - 1_{11}$ and $2_{11} - 2_{12}$ transitions.

Some insight into this behaviour can be gained by considering the radiative excitation rates between states within the ladders of lower and upper doublet states ($\Delta J = 1, \Delta K_c = \pm 1$) as well as between the lower to the upper doublet states ($\Delta J = 0, \Delta K_c = \mp 1$). To illustrate this we show the variation of $\tau_{4,8}$ on the specific column density for $W_{\text{HII}} = 0.5, 0.1$, and 0.05 for a free-free radiation field with $\text{EM} = 3.41 \times 10^{10} \text{ pc cm}^{-6}$ in the upper panel of Fig. 7. The values of the other parameters are as shown in the Figure. For a maser pathlength of $7 \times 10^{16} \text{ cm}$ (at the specific column density indicated by vertical dashed line in the upper panel; see Section 4.2) it is seen that $|\tau_{4,8}|_{W_{\text{HII}}=0.5} < |\tau_{4,8}|_{W_{\text{HII}}=0.1} < |\tau_{4,8}|_{W_{\text{HII}}=0.05}$. Calculation of the radiative excitation rates for the $\Delta J = 1, \Delta K_c = 1$ transitions when $W_{\text{HII}} = 0.5$, gives rates between $\sim 0.019 \text{ s}^{-1}$ and $\sim 0.023 \text{ s}^{-1}$. This translates to characteristic ‘lifetimes’ for a H_2CO molecule in the lower states of these transitions to be between 42 and 51 seconds. The corresponding transition rates for a molecule in the ladder of lower doublet states to make a transition to the associated upper doublet state ($\Delta J = 0, \Delta K_c = -1$) fall between $6 \times 10^{-5} \text{ s}^{-1}$ and $8 \times 10^{-4} \text{ s}^{-1}$, which translates to characteristic lifetimes between 1250 and 16700 seconds. The effect of the much higher transition rates (shorter lifetimes) for $\Delta J = 1, \Delta K_c = 1$ transitions compared to the $\Delta J = 0, \Delta K_c = -1$ transitions is, therefore, that molecules excited into the ladder of lower doublet states will tend to stay in the ladder of lower doublet states with only a small probability of making a transition to the ladder of upper doublet states. Even if there is any population inversion for the $1_{10} - 1_{11}$ transition, the high radiative excitation rate for $1_{10} \rightarrow 2_{11}$ will further tend to reduce the magnitude of the inversion. On the other hand, for $W_{\text{HII}} = 0.05$, the transition rates are an order of magnitude smaller with the characteristic lifetimes

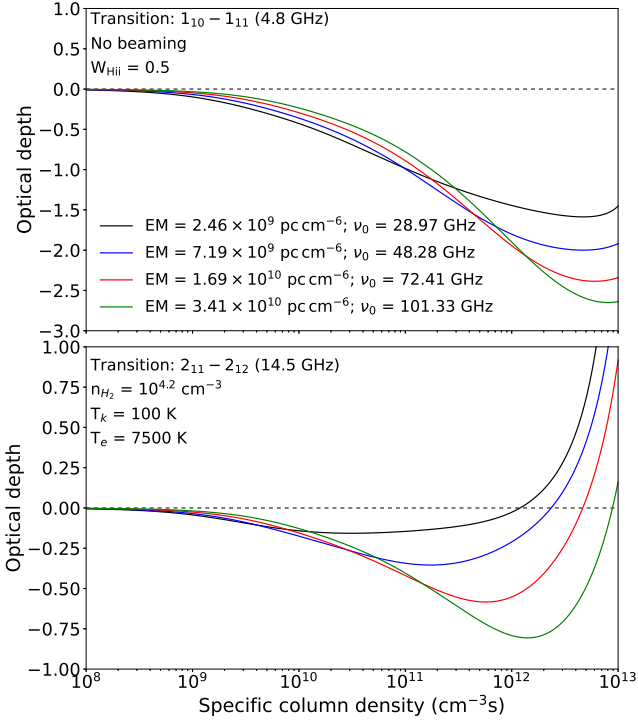


Figure 5. Variation of the optical depths for the $1_{10} - 1_{11}$ (upper panel) and $2_{11} - 2_{12}$ (lower panel) transitions as a function specific column density for the four emission measures and a dilution factor of 0.5 as shown in the upper panel of Fig. 2.

for the $\Delta J = 1, \Delta K_C = 1$ transitions, ranging between 430 and 513 seconds which increases the probability for a molecule in the ladder of lower doublet states to be transferred to the ladder of upper doublet states. The resulting level populations for the two dilution factors for a maser pathlength of 7×10^{16} cm are compared in the bottom panel of Fig. 7. The effect of the higher radiative transition rates for $W_{\text{HII}} = 0.5$ is evidenced in the larger level populations for the higher energy states compared to the case of $W_{\text{HII}} = 0.05$.

4.2 Beaming

Inspection of Figs. 4, 5 and 6 shows that the maximum negative optical depth for the $1_{10} - 1_{11}$ transition is less than -3 , which is too small to account for observed maser brightness temperatures of the order of 10^6 to 10^8 K, even if the masing region is projected against a background source with a brightness temperature of 10^4 K. Fig. 8 compares the variation of $\tau_{4.8}$ (upper panel) and $\tau_{14.5}$ (lower panel) with specific column density when beaming is implemented, according to Eq. 9, for $\alpha = 0$ (no beaming), 1, 5, and 10. The first point to be noted is that, for $\alpha = 5$ and $\alpha = 10$, $\tau_{4.8}$ can be as large as ~ -23 and $\tau_{14.5} \sim -9$. However, these values occur at specific column densities which correspond to maser pathlengths $\sim 8 \times 10^{17}$ cm, which is unrealistically large. Following Boland & de Jong (1981) and Hoffman et al. (2003), the maser pathlength is assumed to be geometrically constrained by the radius of the H II region. Using the data of Meng et al. (2022), an average radius, $\langle R_{\text{HII}} \rangle$, of 4.8×10^{16} cm and with a standard deviation, σ , of 3.0×10^{16} cm, is found for 39 ultra-compact H II regions in Sgr B2. For the present calculations a maser pathlength of 7×10^{16} cm was used which is slightly smaller

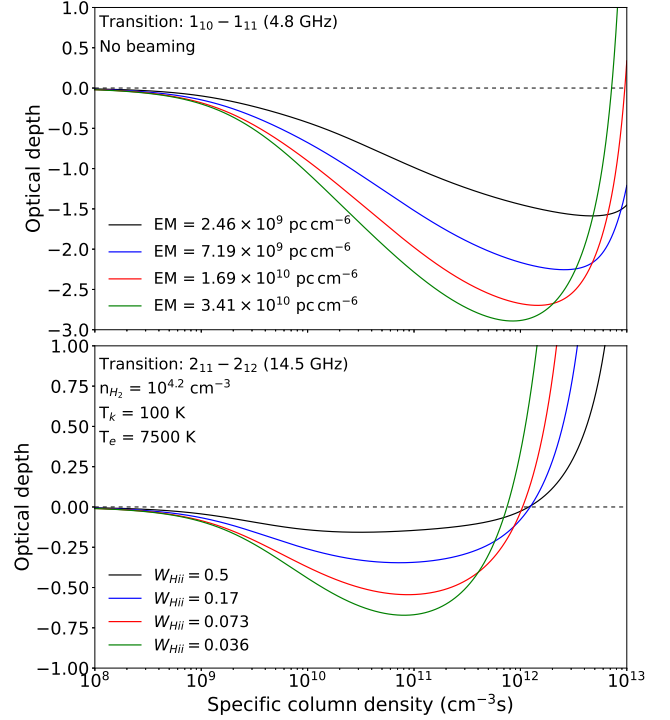


Figure 6. Variation of the optical depths for the $1_{10} - 1_{11}$ (upper panel) and $2_{11} - 2_{12}$ (lower panel) transitions as a function specific column density for the four emission measures and dilution factors as shown in the lower panel of Fig. 2.

than $\langle R_{\text{HII}} \rangle + \sigma$. In Fig. 8 such a maser pathlength corresponds to a specific column density of 1.85×10^{11} cm⁻³ s and is indicated by the black dashed vertical line. At this specific column density $\tau_{4.8}$ has the values $-1.86, -3.81, -7.56, -9.10$ respectively for $\alpha = 0, 1, 5, 10$. The corresponding values for $\tau_{14.5}$ are $-0.77, -1.79, -3.85, -4.69$. These numbers clearly illustrate the effect of beaming.

A striking feature in the behaviour of the optical depths in Fig. 8 is the small but rapid changes in the optical depth with increasing specific column density for $\alpha = 5$ and $\alpha = 10$. For example, it is seen that, for $\alpha = 10$, both the $1_{10} - 1_{11}$ and $2_{11} - 2_{12}$ transitions show a small decrease (becoming less negative) in optical depth at a specific column density of 10^{12} cm⁻³ s, after which it further increases (becoming more negative) again. While this behaviour might at first appear odd when compared with the smooth variation of the optical depth as shown in Figs. 5 and 6, in fact, it reflects the coupling between the doublet states of o-H₂CO. This behaviour is further illustrated in Fig. 9 where the variation of the optical depth as a function of specific column density is shown for the first five doublet transitions as indicated in the graph. All five transitions are inverted at very small specific column densities. The $5_{14} - 5_{15}$ transition (dashed black line) is the first to switch from inversion to non-inversion, followed by $4_{13} - 4_{14}$ (green) and $3_{12} - 3_{13}$ (red) at larger specific column densities. It is seen that when a higher J doublet switches from being inverted to non-inverted it has the effect to create a small ‘‘bump’’ in the optical depths of the inverted lower J doublets. To understand the origin of this effect, we show in Fig. 10 the behaviour of $n_{\text{lower}}/n_{\text{upper}}$ for the $1_{10} - 1_{11}$, $2_{11} - 2_{12}$ and $3_{12} - 3_{13}$ transitions for specific column densities between $3.7 - 3.9 \times 10^{12}$ cm⁻³ s. A transition is inverted when $n_{\text{lower}}/n_{\text{upper}} < g_{\text{lower}}/g_{\text{upper}}$, while keeping in mind that $g_{\text{upper}} = g_{\text{lower}}$ for the doublet transitions. The

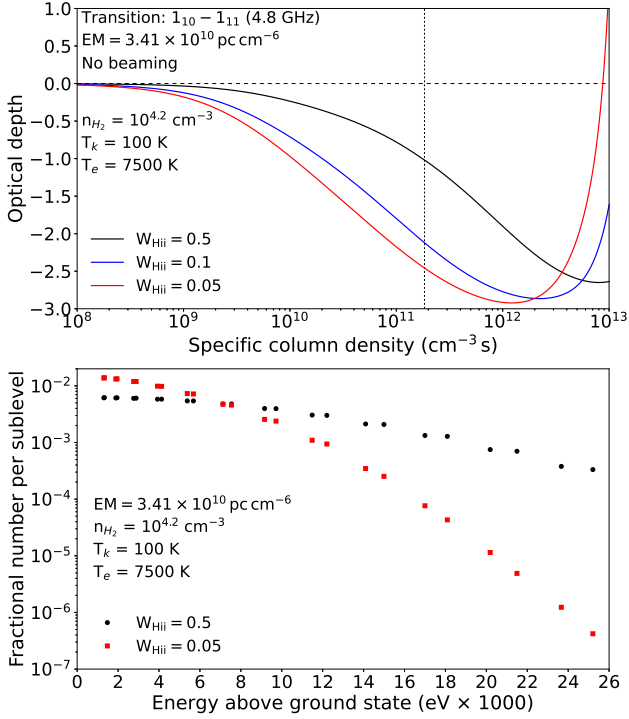


Figure 7. *Upper panel:* Variation of the optical depth of the $1_{10} - 1_{11}$ transition to illustrate the behaviour of $\tau_{4.8}$ for different dilution factors. The vertical dashed line is located at a specific column density of $1.8 \times 10^{11} \text{ cm}^3 \text{ s}^{-1}$ which corresponds to a maser pathlength of $7 \times 10^{16} \text{ cm}$ for $n_{\text{H}_2} = 10^{4.2} \text{ cm}^{-3}$, a H_2CO abundance of 5×10^{-6} and, a velocity width of 300 m s^{-1} . *Lower panel:* Solution for the level populations at a maser pathlength of $7 \times 10^{16} \text{ cm}$ for the dilution factors as shown on the graph.

$3_{12} - 3_{13}$ transition switches from inversion to non-inversion at a specific column density of $3.807 \times 10^{12} \text{ cm}^3 \text{ s}$, indicated by the vertical dashed black line. It is seen that there is a rapid increase in $n_{3_{13}}/n_{3_{12}}$ after switching from inversion to non-inversion which is due to $n_{3_{13}}$ increasing faster than $n_{3_{12}}$ as the specific column density increases. Since the $4_{13} - 4_{14}$ transition is not inverted anymore at this specific column density, it means that $n_{4_{14}} > n_{4_{13}}$. Furthermore, since the spontaneous decay rates between the lower levels of the doublet states are greater than between the corresponding upper levels, it follows that 3_{13} is populated faster than 3_{12} which explains the rapid increase in $n_{3_{13}}/n_{3_{12}}$ after inversion. Similarly, the spontaneous decay rate for $3_{13} \rightarrow 2_{12}$ is greater than that for $3_{12} \rightarrow 2_{11}$, which means that 2_{12} is populated slightly faster than 2_{11} . This gives rise to a slight decrease in the inversion of the $2_{11} - 2_{12}$ transition and therefore to the decrease of $\tau_{14.5}$ associated with the switching from inversion to non-inversion of the $3_{12} - 3_{13}$ transition. The behaviour of $\tau_{4.8}$ follows directly from similar reasons as for $\tau_{14.5}$. The important point of this behaviour is that it illustrates the coupling between the doublet states and how changes from inversion to non-inversion, and vice versa, of a higher J doublet state affects doublet states at lower J . The reason why this behaviour is present only for stronger beaming can easily be argued from the effect that beaming has on the escape probability for inverted transitions and therefore on the level populations which, in turn, determines the source function and therefore the internal radiation field.

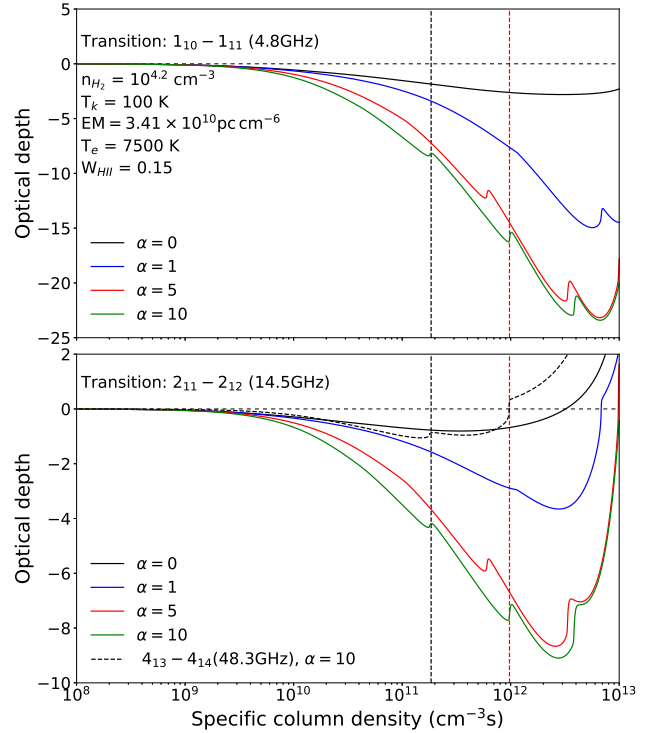


Figure 8. Illustration of the effect of beaming on the optical depth of the $1_{10} - 1_{11}$ and $2_{11} - 2_{12}$ transitions. The parameters for the calculation are shown in the upper panel. The red dashed vertical line indicates the specific column density where the $4_{13} - 4_{14}$ transition (48 GHz) switches from being inverted to non-inverted. The black dashed vertical line indicates the specific column density where the maser pathlength equals $7 \times 10^{16} \text{ cm}$.

4.3 Variation of $\tau_{4.8}$ and $\tau_{14.5}$ on the $n_{\text{H}_2} - T_k$ plane

Figures 11–14 show a small selection of examples of the variation of $\tau_{4.8}$ and $\tau_{14.5}$ on the $n_{\text{H}_2} - T_k$ plane that illustrate the typical variation of these two quantities. The maser pathlength used for these results was $7 \times 10^{16} \text{ cm}$. It is seen that, in the presence of a free-free radiation field, inversion of the $1_{10} - 1_{11}$ and $2_{11} - 2_{12}$ transitions can occur over almost the whole of the $n_{\text{H}_2} - T_k$ plane for $50 \leq T_k \leq 300 \text{ K}$ and $10^4 \leq n_{\text{H}_2} \leq 10^6 \text{ cm}^{-3}$. The regions in white on the $n_{\text{H}_2} - T_k$ plane should not be interpreted as implying that there is no inversion; in these regions inversion occurs at maser pathlengths less than $7 \times 10^{16} \text{ cm}$ with $\tau_{4.8}$ and $\tau_{14.5}$ being less than 1. It is interesting to note that for $\text{EM} = 2.46 \times 10^9 \text{ pc cm}^{-6}$ the contours for $\tau_{4.8} > 5$ (upper panel of Fig. 11) are almost independent of the gas kinetic temperature and that the largest values of $\tau_{4.8}$ occur at lower H_2 densities. The pattern changes significantly when $\text{EM} = 3.41 \times 10^{10} \text{ pc cm}^{-6}$ (Figs. 12 and 13). The largest optical depths for $\tau_{4.8}$ now are from -9 to -15 and are found at $T_k \lesssim 100 \text{ K}$ and $n_{\text{H}_2} \lesssim 6 \times 10^4 \text{ cm}^{-3}$. As a further comparison with the upper panel of Fig. 11, the $\tau_{4.8} = 5$ contour, for example, has shifted to higher H_2 densities. An important aspect to note in the bottom panels of Figs. 12 and 13 is that $\tau_{14.5} > -2$ over most of the region where the $2_{11} - 2_{12}$ transition is inverted and even have values > -6 .

The behaviour of $\tau_{4.8}$ and $\tau_{14.5}$ as shown in Figs. 11–13 is typical for other values of the emission measure, beaming parameter, dilution factor and $X_{\text{H}_2\text{CO}} = 5 \times 10^{-6}$. Recent estimates of the H_2CO abundance relative to H_2 for 36 hot molecular cores (Taniguchi et al.

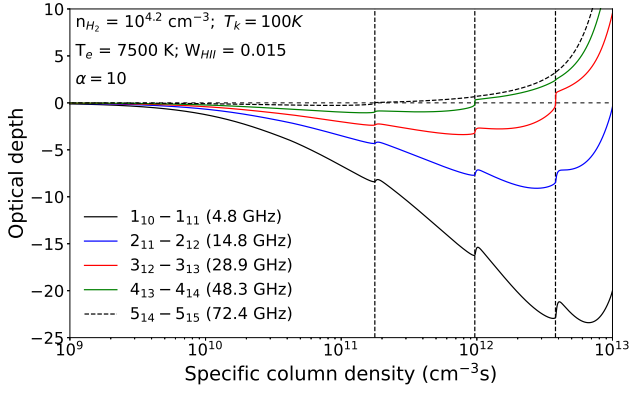


Figure 9. Illustration of the effect of beaming on variation of the optical depth of the first five doublet states. The parameters for the calculation are shown in the graph. From left to right the dashed vertical lines indicate the specific column densities where, respectively, the $4_{13} - 4_{14}$, $3_{12} - 3_{13}$, and $2_{11} - 2_{12}$ transitions switch from being inverted to not inverted.

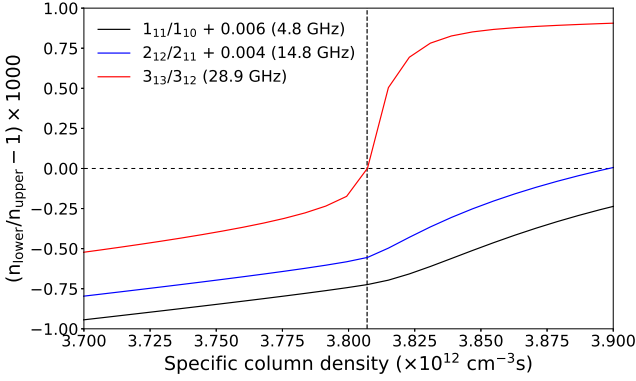


Figure 10. Illustration of the change in the ratio, $n_{\text{lower}}/n_{\text{upper}}$, of populations of the lower to upper levels for the $1_{10} - 1_{11}$, $2_{11} - 2_{12}$ and, $3_{12} - 3_{13}$ transitions around the specific column density where the $3_{12} - 3_{13}$ transition switches from inversion to non-inversion at the position indicated by the dashed vertical line.

2023), points to abundances ranging between $\log X_{\text{H}_2\text{CO}} = -8.68$ and $\log X_{\text{H}_2\text{CO}} = -6.02$ with $\log \overline{X_{\text{H}_2\text{CO}}} = -7.23$, which translates to a value of 5.8×10^{-8} . In Fig. 14 we show the variation of $\tau_{4.8}$ on the $n_{\text{H}_2} - T_k$ plane for H_2CO abundances of 5×10^{-7} and 5×10^{-8} to illustrate the effect of having one and two orders of magnitude smaller abundances. Even with a beaming parameter of $\alpha = 20$ and a dilution factor of 0.3, it is seen that $\tau_{4.8}$ is significantly smaller than when $X_{\text{H}_2\text{CO}} = 5 \times 10^{-6}$.

5 COMMENTS ON CRITIQUE AGAINST FREE-FREE RADIATIVE PUMPING

The results presented above are in principle the same as that of Boland & de Jong (1981), i.e. that the $1_{10} - 1_{11}$ transition can be inverted by a free-free radiation field. Although the results presented above are a significant extension beyond the work of Boland & de Jong (1981), the same criticism raised against the model

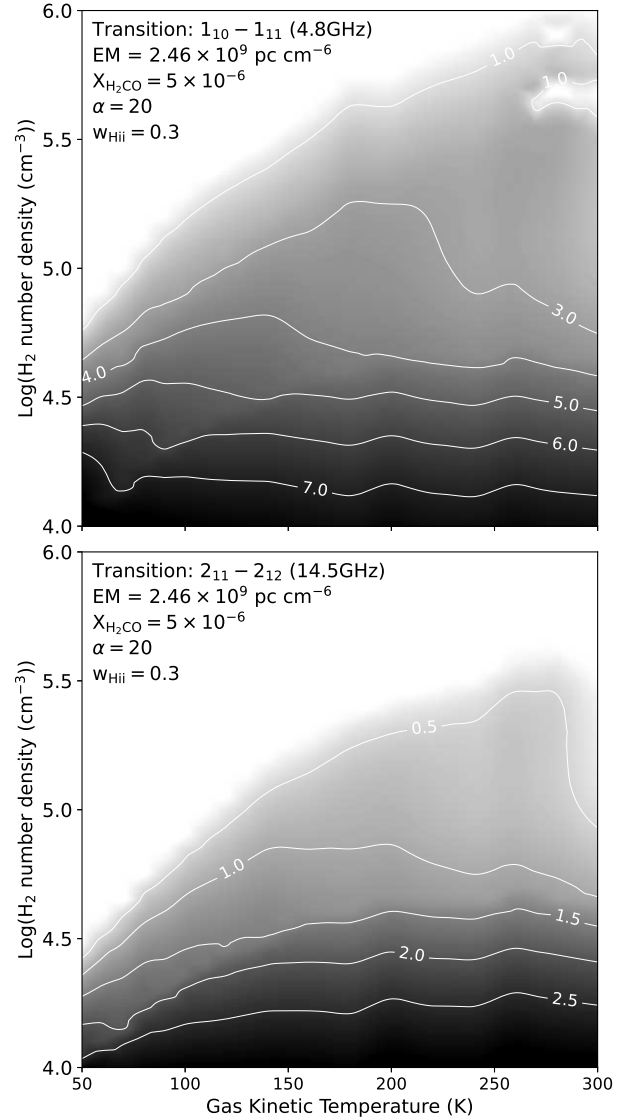


Figure 11. Example of the variation of $|\tau_{4.8}|$ (upper panel) and $|\tau_{14.5}|$ (bottom panel) on the $n_{\text{H}_2} - T_k$ plane for $\text{EM} = 2.46 \times 10^9 \text{ pc cm}^{-6}$ and $\alpha = 20$. The case for $\alpha = 10$ does not differ substantially from what is shown.

of Boland & de Jong (1981), may therefore be raised against the results presented here. We, therefore, comment here on a number of points of critique which have been raised against the free-free radiative pumping of the H_2CO masers.

(i) *The emission measures of the associated H II regions are too small:* The validity of the model of Boland & de Jong (1981) has been questioned by e.g. Pratap et al. (1994), Mehringer et al. (1994) and Araya et al. (2005) on the basis of the emission measures of the associated H II regions being too small. The fact that a significant number of H_2CO masers are found in the vicinity of H II regions, and that the results of the numerical calculations presented above suggest that these masers may be pumped radiatively by a free-free radiation field, raises the question of whether “the problem” is with the pumping scheme or with estimating the emission measures of the H II regions associated with 4.8 GHz H_2CO masers. To illustrate that the observationally derived emission measure of an H II region can differ

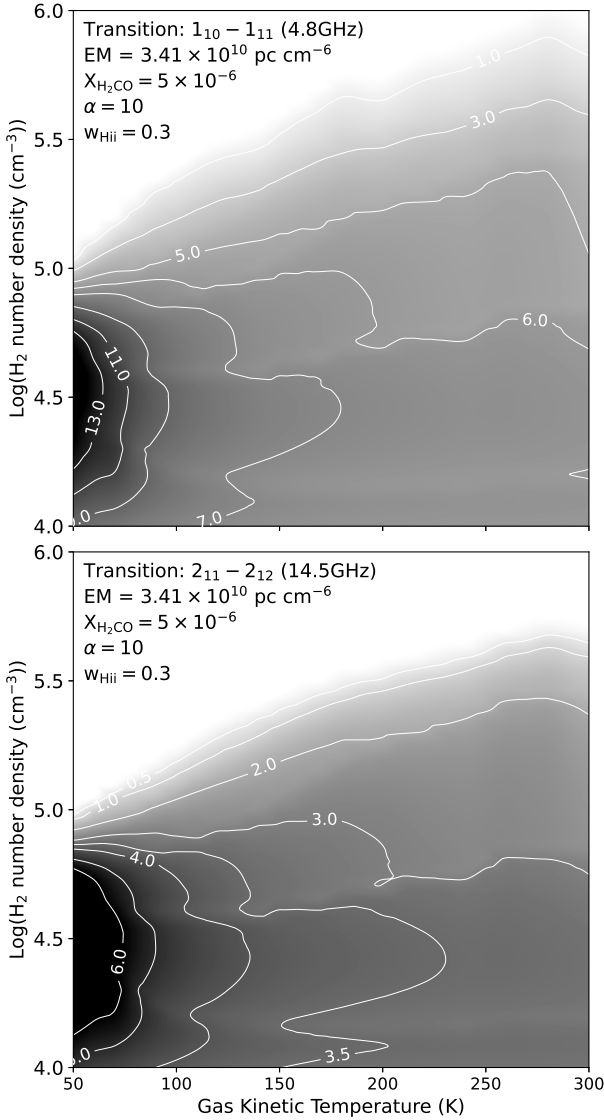


Figure 12. Example of the variation of $|\tau_{4,8}|$ (upper panel) and $|\tau_{14,5}|$ (bottom panel) on the n_{H_2} - T_k plane for $\text{EM} = 3.41 \times 10^{10} \text{ pc cm}^{-6}$ and $\alpha = 10$.

significantly from the real emission measure, the method followed by Meng et al. (2022) to determine the emission measures of H II regions in Sgr B2, was applied to a synthetic H II region calculated with the photo-ionization code Cloudy (Ferland et al. 2017). The following parameters were used in the Cloudy calculation: Blackbody temperature = 35900 K, total luminosity = $10^{38.645} \text{ erg s}^{-1}$, inner radius = $10^{12.845} \text{ cm}$, outer radius = $10^{16.7} \text{ cm}$. The radial dependence of the H I density followed the power law

$$n(r) = n_o(r_o) \left(1 + \frac{\Delta r}{R_s}\right)^\alpha \text{ cm}^{-3}$$

where Δr is the distance from the inner radius, and R_s the scale depth. The H I density at the inner radius was $10^{6.5} \text{ cm}^{-3}$, $R_s = 10^{15.3} \text{ cm}$, and $\alpha = -0.7$. The emission measure was calculated from the resulting radial electron density distribution and was found to be $1.2 \times 10^{10} \text{ pc cm}^{-6}$.

To estimate the emission measures of the H II regions in Sgr

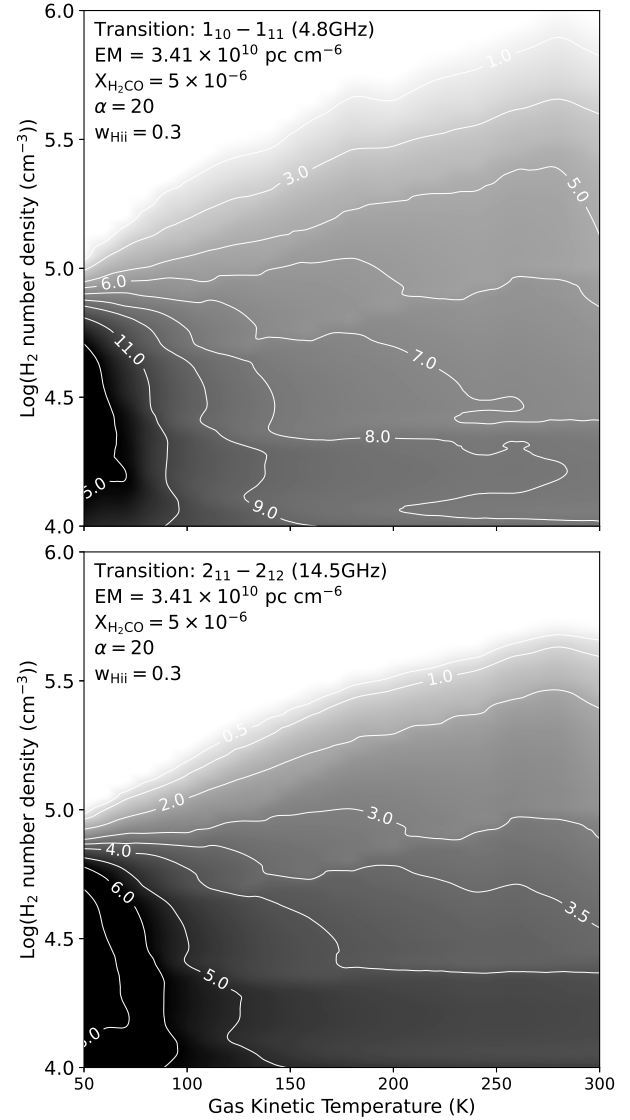


Figure 13. Same as for Fig. 12 but for $\alpha = 20$.

B2, which contains roughly half of the known H₂CO masers in the Galaxy, Meng et al. (2022) used the observed 6 GHz and 22.4 GHz flux densities. Following Meng et al. (2022), the observed flux density is related to the actual radius and emission measure of the H II region according to

$$\frac{S_\nu}{\text{mJy}} = 8.183 \times 10^{-4} \left(\frac{r_{\text{calc}}}{\text{arcsec}}\right)^2 \left(\frac{\nu}{\text{GHz}}\right)^2 \left(\frac{T_e}{\text{K}}\right) (1 - e^{-\tau_\nu}) \quad (12)$$

where the optical depth τ_ν is

$$\tau_\nu = 8.235 \times 10^{-2} \left(\frac{\nu}{\text{GHz}}\right)^{-2.1} \left(\frac{T_e}{\text{K}}\right)^{-1.35} \left(\frac{\text{EM}}{\text{pc cm}^{-6}}\right) \quad (13)$$

(see equations 1 and 2 of Meng et al. 2022). With the observed flux densities at 6 GHz and 22.4 GHz, i.e. S_6 and $S_{22.4}$, there are two equations with two unknowns which have to be solved for r_{calc} and EM. The solution for EM can be obtained by taking the ratio $S_{22.4}/S_6$,

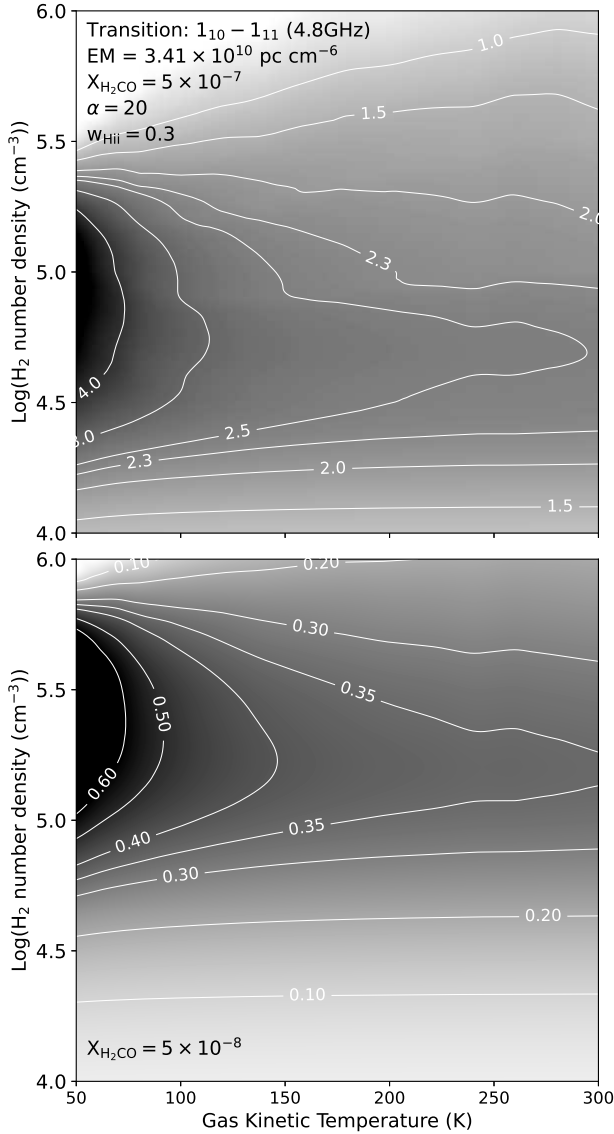


Figure 14. Same as in the upper panel for Fig. 12 but for (a) $X_{\text{H}_2\text{CO}} = 5 \times 10^{-7}$ in the upper panel and (b) $X_{\text{H}_2\text{CO}} = 5 \times 10^{-8}$ in the lower panel.

which, after inserting the numerical values, gives

$$\frac{S_{22.4}}{S_6} = 13.938 \frac{1 - \exp(-k_1 \text{EM})}{1 - \exp(-k_2 \text{EM})} \quad (14)$$

with $k_1 = 4.7878 \times 10^{-10}$ and $k_2 = 7.6128 \times 10^{-9}$ with units of $\text{pc}^{-1} \text{cm}^6$.

In the upper panel of Fig. 15, we show the variation of the optical depth at 6 GHz and 22.4 GHz, calculated from the outer boundary of the synthetic H II region inwards as a function of the emission measure, also calculated from the outer boundary inwards. For 6 GHz, the optical depth reaches a value of 1 at an emission measure of $1.53 \times 10^8 \text{ pc cm}^{-6}$ and for 22.4 GHz at an emission measure of $2.03 \times 10^9 \text{ pc cm}^{-6}$. The fact that the emission at 6 GHz and 22.4 GHz originate from regions with different emission measures (both less than the true emission measure) is already an indication that an estimate of the true emission measure must result in an emission measure which is smaller than the true emission measure.

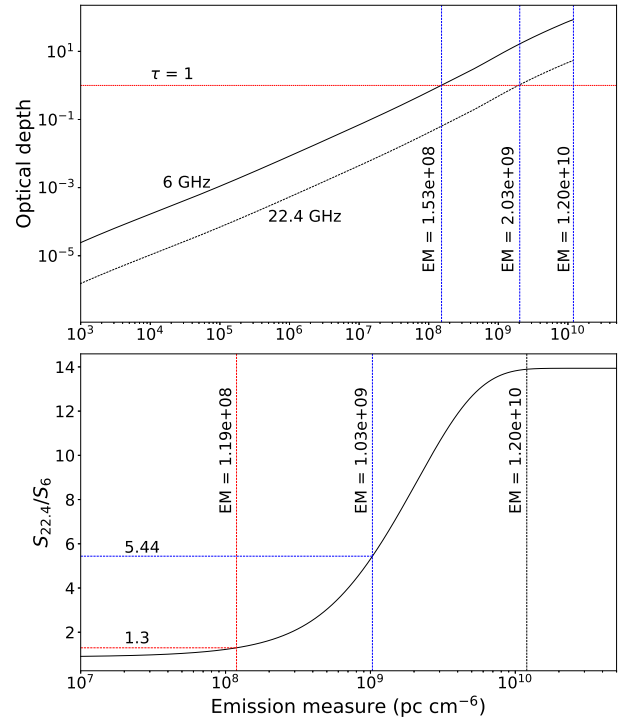


Figure 15. Upper panel: Optical depths at 6 GHz (black solid line) and 22.4 GHz (black dashed line) as a function of emission measure where both quantities are calculated inwards from the outer boundary. Lower panel: Variation of the ratio $S_{22.4}/S_6$ as a function of the emission measure.

Estimating the emission measure using the method of Meng et al. (2022) is shown graphically in the lower panel of Fig. 15. The S-shaped solid line represents the ratio $S_{22.4}/S_6$ as a function of the emission measure according to Eq. 14. From the emitted spectrum of the synthetic H II region, it is found that $S_{22.4}/S_6 = 5.44$, which corresponds to an emission measure $\approx 1.0 \times 10^9 \text{ pc cm}^{-6}$ as indicated on the figure. This is slightly more than an order of magnitude smaller than the true emission measure of the synthetic H II region. The red dashed lines in Fig. 15 are for source number 5 in Tables B1 and B2 of Meng et al. (2022), which is used as verification. For this source $S_{22.4}/S_6 = 1.3$ and the emission measure quoted by Meng et al. (2022) is $1.19 \times 10^8 \text{ pc cm}^{-6}$. It is seen that the solution falls on the line representing Eq. 14.

The implication of the above example for evaluating the current results, but also that of Boland & de Jong (1981), is that some of the H II regions associated with H₂CO masers may have emission measures significantly larger than what has been estimated. Rejection of the free-free pumping of the masers on the basis that the emission measures of the associated H II regions are too small has, therefore, itself to be assessed more critically. Inspection of the emission measures derived by Meng et al. (2022) shows that there are five H II regions with emission measures greater than 10^9 pc cm^{-6} . If, for all five of these cases, the emission measures were underestimated by one order of magnitude, it would mean that their sample contains five H II regions with emission measures greater than $10^{10} \text{ pc cm}^{-6}$ which would significantly change the distribution of emission measures as shown in their Fig. 4. It is interesting to note that from 3-D modelling of the thermal dust and free-free emission in Sgr B2, Schmiedeke et al. (2016) found five H II regions with emission

measures between 1.3×10^{10} and 3.7×10^{10} pc cm $^{-6}$. The reader is referred to Section 3.5 of [Schmiedeke et al. \(2016\)](#) where these authors also point out that the emission measures and electron densities are underestimated for optically thick H II regions.

(ii) *The masers are located too far from the nearest H II region or has no associated continuum source:* The model of [Boland & de Jong \(1981\)](#) requires that the masing region be located at the edge of an H II region. Quite a number of detected H₂CO masers are not projected against an H II region but are offset from an H II region e.g. in G29.96-0.02 ([Pratap et al. 1994](#)) and NGC 7538 ([Andreev et al. 2017](#)), or have no associated continuum source, for example, in Sgr B2 ([Mehringer et al. 1994](#); [Hoffman et al. 2007](#)). Using the same values for n_{H_2} , T_k and T_e as in Fig. 8, the behaviour of the optical depth for the $1_{10} - 1_{11}$, $2_{11} - 2_{12}$, $3_{12} - 3_{13}$ and $4_{13} - 4_{14}$ transitions as a function of radial distance from the centre of the H II region was examined. This was done for $\alpha = 10$, for $\text{EM} = 3.41 \times 10^{10}$ pc cm $^{-6}$ and $\text{EM} = 2.46 \times 10^9$ pc cm $^{-6}$, and for a maser pathlength of 7×10^{16} cm. The results are shown in Fig. 16. First, comparing the behaviour of $\tau_{4.8}$ for the two emission measures, it is seen that for $\text{EM} = 3.41 \times 10^{10}$ pc cm $^{-6}$, inversion occurs over the interval $1 \leq r/R_{\text{HII}} \leq 6$ with $\tau_{4.8}$ having its maximum value at $r/R_{\text{HII}} \simeq 1.3$. For $\text{EM} = 2.46 \times 10^9$ pc cm $^{-6}$, the maximum for $\tau_{4.8}$ is at $r/R_{\text{HII}} = 1$ and inversion occurs only up to $r/R_{\text{HII}} \sim 3$. Considering the $2_{11} - 2_{12}$, $3_{12} - 3_{13}$ and $4_{13} - 4_{14}$ transitions, it is seen, for $\text{EM} = 3.41 \times 10^{10}$ pc cm $^{-6}$, that the maximum r/R_{HII} up to which there is inversion becomes progressively smaller from the $2_{11} - 2_{12}$ to $3_{12} - 3_{13}$ to $4_{13} - 4_{14}$ transitions. For $\text{EM} = 2.46 \times 10^9$ pc cm $^{-6}$ it is only the $1_{10} - 1_{11}$ and $2_{11} - 2_{12}$ transitions that show significant inversion for $r/R_{\text{HII}} < 3$.

The results presented in Fig. 16 show that inversion of the $1_{10} - 1_{11}$ transition can occur for distances from the centre of the H II region of up to six times the radius of the H II region. That some H₂CO masers are not projected onto or at the edge of an H II region does not seem to be a reason to dismiss the pumping of the masers by the free-free continuum radiation field.

It is also not necessary to invoke the possibility of some as yet unknown mechanism for the pumping of the H₂CO masers in Sgr B2 which are not associated with a continuum source. Specific examples are those of masers B and E in Sgr B2, which appear to be “located in regions devoid of continuum emission” ([Mehringer et al. 1994](#)) (see also Fig. 1 of [Hoffman et al. 2007](#)). However, using the coordinates of the two masers as listed by [Hoffman et al. \(2007\)](#), it is found that maser B is located $0''.72$ from the methanol maser MMB G0.672-0.031 ([Caswell et al. 2010](#)) and maser E is associated with the 6.7 GHz methanol maser MMB G0.645-00.042 with an angular separation of $0''.36$ ([Caswell et al. 2010](#)). For maser E the primary peak in the H₂CO maser spectrum is at 49 km s^{-1} ([Mehringer et al. 1994](#)) and for the methanol maser it is at 49.5 km s^{-1} ([Caswell et al. 2010](#)). Both the class II methanol and 4.8 GHz H₂CO masers are exclusively associated with high-mass star forming regions ([Breen et al. 2013](#); [Araya et al. 2007, 2015](#)) which means that both these masers point to as yet undetected high mass star forming regions. Inspection of the 3mm maps of Sgr B2 ([Ginsburg et al. 2018](#)) shows that both masers B and E are associated with faint 3mm continuum sources.

(iii) *The case of IRAS18566+0408 (G37.55+0.20)*

[Araya et al. \(2007\)](#) considered the applicability of the [Boland & de Jong \(1981\)](#) model, i.e., whether population inversion by free-free emission, can explain the H₂CO maser in IRAS 18566+0408 (G37.55+0.20). These authors observed this high mass star forming region with the VLA at 6, 3.6, 1.3, and 0.7 cm. The observed SED was fitted with a combination of optically thin thermal dust emission plus optically thin free-free emission from an ionized

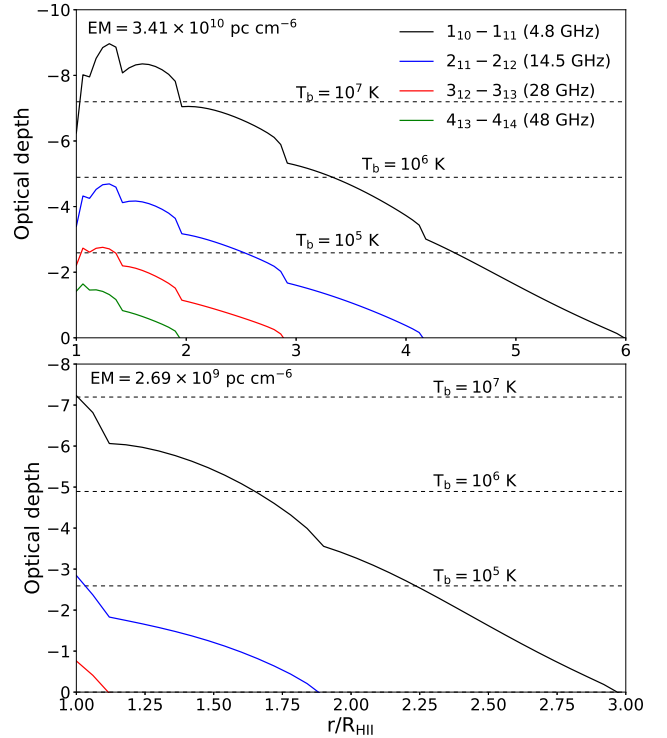


Figure 16. *Upper panel:* Dependence of the optical depths of the first four doublet states as a function of r/R_{HII} for $\text{EM} = 3.41 \times 10^{10}$ pc cm $^{-6}$. The three dashed horizontal lines indicate theoretical brightness temperatures assuming $T_b = 7500 \exp |\tau|$. *Lower panel:* Same as for the upper panel but for $\text{EM} = 2.69 \times 10^9$ pc cm $^{-6}$.

jet (see Fig. 2 of [Araya et al. 2007](#)). Based on the observed SED, [Araya et al. \(2007\)](#) concluded that “excitation by radio continuum is not a feasible mechanism with which to explain the maser in IRAS 18566+0.0408”.

It is, however, necessary to keep in mind that, due to wavelength dependent optical depth effects, the SED of the radiation field at the location of the maser is not necessarily the same as the observed SED. Although there seems to be no detectable H II region associated with IRAS 18566+0408, it does not mean that no highly compact H II region is present. [Keto & Klaassen \(2008\)](#) concluded that “an accreting star begins to produce an H II region once the star reaches a mass, temperature, and luminosity equivalent to early B, about 15 - 20 M_{\odot} ”. If, as remarked by [Araya et al. \(2007\)](#), IRAS 18566+0408 is powered by a single O8 type star (30.8 M_{\odot} , [Sternberg et al. 2003](#)), it seems unlikely that *no* H II region has been excited by the 30 M_{\odot} star. According to [Keto \(2007\)](#) an H II region forms if the ionizing photon rate exceeds the hydrogen accretion rate. Consider then, for example, the simplified case of an O8 star spherically accreting matter at a rate of $10^{-5} M_{\odot} \text{ yr}^{-1}$. This corresponds to a hydrogen accretion rate of $3.8 \times 10^{44} \text{ s}^{-1}$ over the surface of the star. For an O8 star, the ionizing photon rate is $10^{48.75} = 5.62 \times 10^{48} \text{ s}^{-1}$, which is a factor of 1.5×10^4 greater than the hydrogen accretion rate. A young hypercompact H II region with, say, $\text{EM} \gtrsim 10^{10}$ pc cm $^{-6}$, $T_e = 10^4$ K, might thus exist but its mm/sub-mm wavelength emission may be undetectable due to the strong dust emission. The turnover frequency of the free-free emission for such an H II region is ≈ 55 GHz, which implies it also is highly optically thick at centimetre wavelengths (see e.g. [Pratap et al.](#)

1992; Tanaka et al. 2016). However, the continuum radiation field of such an H II region can still be the dominant radiation field within a couple of H II region radii and be responsible for the pumping of the H₂CO masers.

It is also noted that using values of the electron density, electron temperature and physical dimension of the jet as given by Araya et al. (2007), the emission measure for the jet is found to be $2.6 \times 10^6 \text{ pc cm}^{-6}$. This is about three orders of magnitude less than the case of $EM = 2.46 \times 10^9 \text{ pc cm}^{-6}$ which we have considered above. The implication is that the radiative excitation rates from 1_{11} into the ladder of lower doublet states as well as the transition rates within the ladder of lower doublet states is even less than that for the far-infrared dust radiation field (Fig. 2). It can therefore be concluded that the maser is not associated with the jet.

(iv) *The inversion of the $1_{10} - 1_{11}$ transition is due to a rare collisional excitation:* Based on the work of Hill & Hollenbach (1978), Hoffman et al. (2003) proposed that the rarity of the H₂CO masers may be related to a small number of H II regions for which the dissociation wave and the ionization shock wave evolve separately to create a shock/dissociation transition region in which rare transient species are produced. Within this scenario, the inversion of the $1_{10} - 1_{11}$ transition is the achieved through the collision of H₂CO with such a rare species. Hoffman et al. (2003) did not state what this rare molecule or “hot” atom might be, but if it is rare, its abundance in the transition region must be significantly less than that of H₂ and H I in the transition region. Furthermore, since the photodissociation of H₂CO can be caused by photons with energies greater than about 3.4 eV ($\lambda < 360 \text{ nm}$) (Federman & Allen 1991), the possibility of the photodissociation of H₂CO must therefore also be taken into account.

Even if such a rare transient species is produced, it is reasonable to argue that for such a collisional process to produce an inversion of the $1_{10} - 1_{11}$ transition, the collisional excitation rates between the levels of the lower doublet states ($\Delta J = 1, \Delta K_c = 1$) should be comparable to or larger than the corresponding radiative rates to possibly be the dominant pumping mechanism. The collisional excitation rate (probability per unit time) is given by

$$\Gamma_{lu}^c = n_Z C_{lu} = n_Z \frac{g_u}{g_l} C_{ul} e^{-\Delta E_{ul}/kT_k} \quad (15)$$

where Z indicates the rare species, C_{ul} is the collisional de-excitation coefficient and n_Z the number density of the rare species. Equating the right hand sides of Eqs. 11 and 15 it follows that the collisional de-excitation rate required to have the collisional and radiative rates the same is given by

$$C_{ul} = \frac{1}{n_Z} \frac{c^3}{8\pi h \nu_{ul}^3} A_{ul} U_{ul} e^{\Delta E_{ul}/kT_k} \quad (16)$$

Consider, for example, the case where $EM = 3.41 \times 10^{10} \text{ pc cm}^{-6}$ with $W_{\text{H II}} = 0.036$, as in the upper panel of Fig. 6. Even if the “rare species” has a number density as high as 10^3 cm^{-3} , it is found that C_{ul} must have values ranging from $1.25 \times 10^{-6} \text{ cm}^3 \text{ s}^{-1}$ to $2.67 \times 10^{-6} \text{ cm}^3 \text{ s}^{-1}$ for the first eight $\Delta J = 1, \Delta K_c = 1$ transitions in the lower ladder of doublet states. This is four orders of magnitude larger than the corresponding collisional de-excitation rates for collisions with H₂ which will indeed require a very special collision partner for H₂CO.

(v) *The non-detection of the 14.5 GHz maser* As pointed out, the numerical results presented above suggest that under most physical conditions, the 14.5 GHz maser should accompany the detection of the 4.8 GHz maser. Authors such as, for example Hoffman et al. (2003), explicitly searched for 14.5 GHz maser emission toward NGC 7538 and G29.96-0.02. According to these authors their surveys of

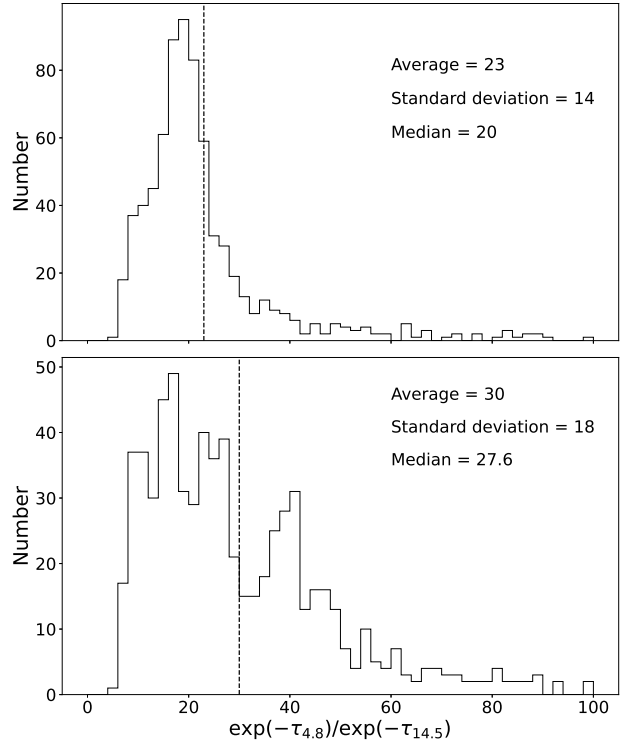


Figure 17. Histograms to show the distribution of the ratio $\exp(-\tau_{4.8})/\exp(-\tau_{14.5})$. The upper panel is for the case shown in Fig. 12 and the lower panel for Fig. 13. The vertical dashed lines indicate the average values.

these two star forming regions had a 3σ brightness temperature sensitivity of 43 K and that a 14.5 GHz maser with $\tau = -1$ would produce an emission line of brightness temperature greater than 100 K. On the basis of this non-detection, Hoffman et al. (2003) concluded that there is no inversion of the $2_{11} - 2_{12}$ transition in these two sources. All the results presented above indicate that, in the presence of a free-free radiation field, the $2_{11} - 2_{12}$ transition should be inverted, as was also found by Boland & de Jong (1981). It is difficult to see, for example, how to have $\tau_{4.8} \gtrsim -5$ while there is no inversion of the $2_{11} - 2_{12}$ transition, especially when beaming plays a role. Inversion of the $2_{11} - 2_{12}$ and higher J doublet transitions can be reduced by increasing the escape probability for these transitions. This can be done, for example, by also setting $\Omega_\nu(\tau_\nu) \propto (\nu/\nu_0)^\delta$, where $\nu_0 = 4.8 \text{ GHz}$. However, due to the coupling of the doublet states as described above, the effect of doing this was found to also reduce the inversion of the $1_{10} - 1_{11}$ transition.

In spite of the fact that the $2_{11} - 2_{12}$ transition is almost always inverted when the $1_{10} - 1_{11}$ transition is inverted, it is worth noting that the brightness temperature of the 14.5 GHz maser can be considerably less than that of the 4.8 GHz maser. To illustrate this, we first show in Fig. 17 the distribution of $\exp(-\tau_{4.8})/\exp(-\tau_{14.5})$ for the cases presented in Figs. 12 and 13 for $\exp(-\tau_{4.8})/\exp(-\tau_{14.5}) < 100$. The average, standard deviation and median as shown in both panels were calculated only for $\exp(-\tau_{4.8})/\exp(-\tau_{14.5}) < 100$, since the fewer very large values (> 1000) considerably skew the average and standard deviation from the main distribution. For unsaturated gain, the distributions as shown in the upper and lower panels also reflect the ratio of the brightnesses of the two masers for equal background intensities or brightness temperatures. Comparison of the two

distributions suggest that stronger beaming ($\alpha = 20$ (lower panel) compared to $\alpha = 10$ (upper panel)) shifts the average 23 to 30, suggesting that stronger beaming acts in favour of the 4.8 GHz maser.

However, the non-detection of the 14.5 GHz maser cannot be explained even for $\exp(-\tau_{4.8})/\exp(-\tau_{14.5}) = 100$. Apart from the fact that, within the framework of our calculations, $\exp(-\tau_{4.8}) > \exp(-\tau_{14.5})$, projection of the masing region against an H II region might be such that the background brightness temperature at 4.8 GHz ($T_{4.8}$) is greater than at 14.5 GHz ($T_{14.5}$). Quite generally the electron density is a decreasing function of the radial distance from the centre of the H II region. The effective emission measure along a chord offset from the centre of the H II region, decreases with increasing projected distance from the centre of the H II region not only due to a decrease in the electron density but also due to the shorter chord length. The turnover frequency, ν_0 , also shifts to lower frequencies since $\nu_0 \propto EM^{0.476}$. Now $T_b = T_e$ for $\nu \leq \nu_0$ while, as a reasonable approximation, $T_b(\nu) = T_e(\nu_0/\nu)^{-2}$ when $\nu > \nu_0$. Thus, if $\nu_0 \lesssim 1$ GHz, the ratio between the background brightness temperatures at 4.8 and 14.5 GHz is such that $T_{4.8}/T_{14.5} = 9.13$. Considering therefore $T_{4.8} \exp(-\tau_{4.8})/T_{14.5} \exp(-\tau_{14.5}) = 9.13 \exp(-\tau_{4.8})/\exp(-\tau_{14.5})$, it follows from Fig. 17 that the 4.8 GHz maser may be more than two orders of magnitude brighter than the 14.5 GHz maser.

To illustrate this with a numerical example, consider the above results of the Cloudy calculations of a synthetic H II region with $EM = 1.2 \times 10^{10} \text{ pc cm}^{-6}$ and assume the maser to be projected against the H II region at a distance of $4 \times 10^{16} \text{ cm}$ from the centre. From the Cloudy calculations it is found that the electron density at that distance from the centre of the H II region is $\sim 5900 \text{ cm}^{-3}$ and $T_e = 7165 \text{ K}$. For a spherical H II region the corresponding chord length is $6 \times 10^{16} \text{ cm}$ with an average electron density of 5515 cm^{-3} along the chord. Although the true emission measure of the H II region is $1.2 \times 10^{10} \text{ pc cm}^{-6}$, the emission measure of the region against which the maser is projected is $5.9 \times 10^5 \text{ pc cm}^{-6}$, assuming that $n_e = 5515 \text{ cm}^{-3}$ and $T_e = 7165 \text{ K}$ is constant along the length of the chord. The corresponding turnover frequency, ν_0 , for the free-free emission from such a thermal hydrogen plasma is 565 MHz. Using $T_b(\nu_0) = T_e$ we have $T_b(4.8 \text{ GHz}) \approx 99 \text{ K}$ and $T_b(14.5 \text{ GHz}) \approx 10 \text{ K}$. With, for example, $n_{\text{H}_2} = 10^{4.5} \text{ cm}^{-3}$, $T_k = 100 \text{ K}$, $EM = 1.2 \times 10^{10} \text{ pc cm}^{-6}$, beaming factor $\alpha = 10$ and, $W_{\text{H II}} = 0.075$, we find $\tau_{4.8} = 4.9$ and $\tau_{14.5} = 1.3$ for a maser length of $7 \times 10^{16} \text{ cm}$. This gives a 4.8 GHz maser brightness temperature of 13335 K and a 14.5 GHz maser brightness temperature of only 40 K. Although this example cannot be considered as presenting a full explanation of the (apparent) absence of the 14.5 GHz masers, it does illustrate that the brightness temperature of the 14.5 GHz maser can be significantly less than that of the 4.8 GHz maser and that the projection of the masing region against the background H II may be a contributing factor.

6 EVALUATION AND CONCLUSIONS

As stated in the Introduction, the primary aim of this work is to first establish whether the pumping scheme proposed by [van der Walt & Mfulwane \(2022\)](#) is indeed also responsible for the inversion of the $1_{10} - 1_{11}$ transition by a free-free radiation field. The results presented in Section 3 convincingly showed the transfer of molecules from the ladder of lower doublet states to the ladder of upper doublet states is essential to create an inversion of the $1_{10} - 1_{11}$ transition. Since inversion of the $1_{10} - 1_{11}$ transition can also be achieved through collisions alone through the same process ([van der Walt & Mfulwane 2022](#)), it follows that any other proposed

pumping mechanism must operate in the same way, i.e., a faster excitation into the ladder of lower doublet states compared to the ladder of upper doublet states, as well transferring molecules from the ladder of lower doublet states to the ladder of upper doublet states at a rate that will result in an inversion of the $1_{10} - 1_{11}$ transition.

The results presented above clearly indicate that the typical free-free radiation field of an H II region associated with young high mass stars is very effective to invert the $1_{10} - 1_{11}$ and other doublet transitions over a wide range of H_2 densities and kinetic temperatures. Depending on the emission measure of the H II region, inversion can be achieved at distances from the centre of the H II region of up to six times the radius of the H II region. Our results also showed that with beaming, sufficient amplification factors can be achieved. Considering these results, there is, therefore, no reason to question the viability of the pumping of the 4.8 GHz masers by a free-free radiation field. In fact, even though the $1_{10} - 1_{11}$ transition can be inverted by collisions alone, the results clearly indicate that, closer to the H II region, radiative pumping by the free-free radiation field, by far dominates the inversion. The implication is that any other postulated collisional process for the pumping of the masers, will have to compete with the radiative pumping by the free-free radiation field.

As stated in the Introduction, to explain the rarity of the H_2CO masers a distinction must be made between the pumping scheme and other possible factors that determine the number and life-time of the masers. The fact that not only the $1_{10} - 1_{11}$ but also the $2_{11} - 2_{12}$ transition can be inverted over most of the $n_{\text{H}_2} - T_k$ plane would suggest that there should be significantly more H_2CO masers than what has been discovered up to now. There are at least two such external factors that can possibly contribute to the small number of detected H_2CO masers. The first is the rate at which the H II region, and therefore also its emission measure, evolves. As is shown in Fig. 2, excitation from the 1_{11} state into the ladder of lower doublet states is through frequencies in the optically thin part of the spectral energy density distribution. Since for the optically thin part the spectral energy density is proportional to the emission measure, the excitation rates into the ladder of lower doublet states will decrease as the emission measure decreases due to the evolution of the H II region. The evolution of the H II region may therefore affect the life-time and thus the number of H_2CO masers.

Another factor that may play a role in the number of detected H_2CO masers is the H_2CO abundance. It is clear from Fig. 14 that the H_2CO abundance is relevant in determining whether the amplification factor is large enough to produce a detectable maser. Considering again the results of [Taniguchi et al. \(2023\)](#), it is found for the sample of 36 hot cores that $\log X_{\text{H}_2\text{CO}} = -7.23$ and $\sigma = 0.62$. The skewness of the sample is ~ -0.4 which indicates that it is slightly skew toward smaller abundances. Assuming that the distribution of $\log X_{\text{H}_2\text{CO}}$ is Gaussian (for which the skewness is 0), it is found that the probability is 2.4% to find a hot core for which $\log X_{\text{H}_2\text{CO}} > -6$. If the H_2CO and the class II CH_3OH masers are associated with the same population of ~ 1000 high mass star forming regions detected in the MMB survey ([Green & the MMB Survey Collaboration 2012](#)), it follows that there should be about 24 4.8 GHz H_2CO masers if all masers for which $X_{\text{H}_2\text{CO}} > 10^{-6}$ are detectable. This example should not be interpreted as a prediction of the total number of 4.8 GHz H_2CO masers but only to illustrate that external factors which are independent of the pumping scheme, as well as of the pumping mechanism (the free-free radiation field), can lead to a relatively small number of detected maser sources. The number may be even lower if the duration of the masing phase is also affected by the evolution of the H II region.

There are a number of 4.8 GHz H_2CO masers that also have associated 6.7 GHz CH_3OH masers for which there appears to be very good spatial and velocity agreement between the two maser species. Masers B and E in Sgr B2 already referred to above are such examples. A striking example is in the case of G339.98-1.26 where three of the 4.8 GHz H_2CO features correspond in velocity to three of the 6.7 GHz CH_3OH maser features (Chen et al. 2017b). Also in the case of G0.38+0.04 there is very good spatial and velocity agreement between the 4.8 GHz H_2CO and 6.7 GHz CH_3OH masers (Ginsburg et al. 2015). The question then is to what extent there is similarity in the conditions to excite the two maser species. We note the following differences which need to be resolved if these two maser species are to be associated with the same physical and kinematic structures. From Fig.7 of Cragg et al. (2002) it is seen that to explain the brightness temperatures of the order of 10^{12} K of the 6.7 GHz CH_3OH masers requires dilution factors, W_{HII} , to be less than about 10^{-4} . This implies $r \gtrsim 50R_{\text{HII}}$ (Eq. 4) while $r \lesssim 6R_{\text{HII}}$ seems to be required for the 4.8 GHz H_2CO masers (Fig. 16). Cragg et al. (2002) also concluded that the brightest 6.7 GHz CH_3OH masers are found for $10^5 < n_{\text{H}_2} < 10^{8.3} \text{ cm}^{-3}$ with $T_k < T_d > 100$ K. For H_2CO , the results presented above suggest that to have a reasonable amplification factor, e.g. $\tau_{4.8} < -5$, requires $n_{\text{H}_2} < 10^{5.5} \text{ cm}^{-3}$ (Figs. 11 and 12). Although the calculations of Cragg et al. (2002) and those presented here used different numerical methods which may contribute to some of the differences, at face value it would seem, from a theoretical point of view, that the two maser species are not associated with the same physical and kinematic structure in the star formation environment.

Within the context of this discussion, it is has to be pointed out that the 4.8 GHz H_2CO masers which are normally associated with G29.96-0.02, are most likely not associated with the cometary HII region but rather with a hot molecular core (HMC) hosting an object identified as a high mass protostellar object (Cesaroni et al. 1998; De Buizer et al. 2002). Spatially there are three water masers associated with this HMC (Hofner & Churchwell 1996), with one of the 4.8 GHz H_2CO masers located only $0''.18$ from one of the water maser features. Although it is not clear what the exact location of the 4.8 GHz H_2CO maser in the HMC is, the conclusions drawn of it being associated with, and located toward, the edge of the cometary HII region might be different than if it is associated with a young background HMC. The first, obviously, is the different evolutionary states of the star forming region with which the maser is associated which also have consequences regarding the chemical evolution. Different conclusions can also be reached regarding the optical depth required to explain the observed brightness temperature of the maser. In the case of G29.96-0.02, Hoffman et al. (2003) concluded that to explain the observed brightness temperature of $\sim 10^7$ K requires $\tau_{4.8} \approx -12$ based on a 6 cm background temperature of 50 K. From the upper panels of Figs. 12 and 13 it is seen that, within the framework of the current calculations, such optical depths occur only at lower gas kinetic temperatures. However, if the maser is projected against a hypercompact HII region associated with an earlier phase of high mass star formation, the background temperature may be significantly higher. For example, if the background temperature is 5000 K, the optical depth required to explain a brightness temperature of the order of 10^7 K, is ~ -7.6 . It is obvious from Figs. 12 and 13 that in this case a significantly different conclusion is reached about the conditions under which the maser might be excited.

As a last remark we note that, having established that a free-free radiation field is effective to pump the 4.8 GHz H_2CO masers and a far-infrared dust radiation field is not, it follows that the underlying mechanism for the periodic variability of the H_2CO and CH_3OH

masers in IRAS18566+0408 (G37.55+0.20) cannot be due to varying pumping conditions for both maser species. Since the pumping schemes for the two masers are completely different, it would require an impossible degree of fine tuning of variability between the free-free and dust radiation fields for the amplification factors to behave in exactly the same way to produce similar light curves. The flaring must therefore be associated with the source of seed photons, as was argued by van der Walt (2014) and as is strongly suggested by the recent results of Gray et al. (2020, see their Section 6).

ACKNOWLEDGEMENTS

I would like to thank Prof. David Modise, Dean of the Faculty of Natural and Agricultural Sciences, as well as Prof. Francois van der Westhuizen, Deputy Dean (Research) of the Faculty of Natural and Agricultural Sciences of the NWU, for financial support without which this work could not have been done. I also thank an anonymous reviewer for constructive comments to improve the paper.

DATA AVAILABILITY

No new data has been generated in this project.

REFERENCES

- Andreev N., Araya E. D., Hoffman I. M., Hofner P., Kurtz S., Linz H., Olmi L., Lorrain-Costa I., 2017, *ApJS*, **232**, 29
- Araya E., Hofner P., Kurtz S., Linz H., Olmi L., Sewilo M., Watson C., Churchwell E., 2005, *ApJ*, **618**, 339
- Araya E., Hofner P., Goss W. M., Kurtz S., Linz H., Olmi L., 2006, *ApJ*, **643**, L33
- Araya E., et al., 2007, *ApJ*, **669**, 1050
- Araya E. D., Hofner P., Goss W. M., Linz H., Kurtz S., Olmi L., 2008, *ApJS*, **178**, 330
- Araya E. D., Olmi L., Morales Ortiz J., Brown J. E., Hofner P., Kurtz S., Linz H., Creech-Eakman M. J., 2015, *ApJS*, **221**, 10
- Baan W. A., An T., Klöckner H.-R., Thomasson P., 2017, *MNRAS*, **469**, 916
- Boland W., de Jong T., 1981, *A&A*, **98**, 149
- Breen S. L., Ellingsen S. P., Contreras Y., Green J. A., Caswell J. L., Stevens J. B., Dawson J. R., Voronkov M. A., 2013, *MNRAS*, **435**, 524
- Caswell J. L., et al., 2010, *MNRAS*, **404**, 1029
- Cesaroni R., Hofner P., Walmsley C. M., Churchwell E., 1998, *A&A*, **331**, 709
- Chen X., et al., 2017a, *MNRAS*, **466**, 4364
- Chen X., Shen Z.-Q., Ellingsen S. P., Li X.-Q., Yang K., Chen H.-Y., Dong J., 2017b, *ApJ*, **851**, L3
- Cragg D. M., Sobolev A. M., Godfrey P. D., 2002, *MNRAS*, **331**, 521
- De Buizer J. M., Watson A. M., Radomski J. T., Piña R. K., Telesco C. M., 2002, *ApJ*, **564**, L101
- Downes D., Wilson T. L., 1974, *ApJ*, **191**, L77
- Elitzur M., ed. 1992, *Astronomical masers Astrophysics and Space Science Library* Vol. 170
- Federman S. R., Allen M., 1991, *ApJ*, **375**, 157
- Ferland G. J., et al., 2017, *Rev. Mex. Astron. Astrofis.*, **53**, 385
- Gardner F. F., Whiteoak J. B., Forster J. R., Pankonin V., 1986, *MNRAS*, **218**, 385
- Ginsburg A., et al., 2015, *A&A*, **584**, L7
- Ginsburg A., et al., 2018, *ApJ*, **853**, 171
- Gray M. D., Etoke S., Travis A., Pimpanuwat B., 2020, *MNRAS*, **493**, 2472
- Green J. A., the MMB Survey Collaboration 2012, *arXiv e-prints*, p. [arXiv:1210.0979](https://arxiv.org/abs/1210.0979)
- Hill J. K., Hollenbach D. J., 1978, *ApJ*, **225**, 390
- Hoffman I. M., Goss W. M., Palmer P., Richards A. M. S., 2003, *ApJ*, **598**, 1061

- Hoffman I. M., Goss W. M., Palmer P., 2007, *ApJ*, 654, 971
- Hofner P., Churchwell E., 1996, *A&AS*, 120, 283
- Keto E., 2007, *ApJ*, 666, 976
- Keto E., Klaassen P., 2008, *ApJ*, 678, L109
- Martín-Pintado J., Gaume R. A., Rodríguez-Fernández N., de Vicente P., Wilson T. L., 1999, *ApJ*, 519, 667
- McCarthy T. P., et al., 2022, *MNRAS*, 509, 1681
- Mehring D. M., Goss W. M., Palmer P., 1994, *ApJ*, 434, 237
- Meng F., et al., 2022, *A&A*, 666, A31
- Pratap P., Snyder L. E., Batrla W., 1992, *ApJ*, 387, 241
- Pratap P., Menten K. M., Snyder L. E., 1994, *ApJ*, 430, L129
- Schmiedeke A., et al., 2016, *A&A*, 588, A143
- Schöier F. L., van der Tak F. F. S., van Dishoeck E. F., Black J. H., 2005, *A&A*, 432, 369
- Shuvo O. I., Araya E. D., Tan W. S., Hofner P., Kurtz S., Pihlström Y. M., Hoffman I. M., 2021, *MNRAS*, 504, 1733
- Sternberg A., Hoffmann T. L., Pauldrach A. W. A., 2003, *ApJ*, 599, 1333
- Tanaka K. E. I., Tan J. C., Zhang Y., 2016, *ApJ*, 818, 52
- Taniguchi K., et al., 2023, *ApJ*, 950, 57
- Whiteoak J. B., Gardner F. F., 1983, *MNRAS*, 205, 27P
- Wilson T. L., Rohlfs K., Hüttemeister S., 2009, *Tools of Radio Astronomy*, doi:10.1007/978-3-540-85122-6.
- van der Walt D. J., 2014, *A&A*, 562, A68
- van der Walt D. J., Mfulwane L. L., 2022, *A&A*, 657, A63
- van der Walt D. J., Ginsburg A., Goddi C., 2021, *MNRAS*, 501, 3871

This paper has been typeset from a $\text{\TeX}/\text{\LaTeX}$ file prepared by the author.